J. Fluid Mech. (1990), *vol.* 218, *pp.* 171–223
Printed in Great Britain

The effect of anisotropic wall compliance on boundary-layer stability and transition

By PETER W. CARPENTER[1] AND PHILIP J. MORRIS[2]

[1] School of Engineering, University of Exeter, Exeter, EX4 4QF, UK

[2] Department of Aerospace Engineering, The Pennsylvania State University, University Park, PA 16802, USA

(Received 28 July 1989 and in revised form 3 February 1990)

A fairly simple theoretical model of an anisotropic compliant wall has been developed. It has been used to undertake a comprehensive numerical study of boundary-layer stability over such walls. The study is based on linearized theory, makes the usual quasi-parallel-flow approximation, uses the Blasius profile as the basic undisturbed flow and assumes two-dimensional disturbances. An investigation is carried out of the effects of anisotropic wall compliance on the Tollmien–Schlichting waves and the two previously identified wall modes, namely travelling-wave flutter and divergence. In addition global convergence techniques are used to search for other possible instabilities.

An asymptotic theory, valid for high Reynolds numbers, is also presented. This can provide accurate estimates of the eigenvalues. It is applicable to a much wider class of compliant walls than the relatively simple model used for the numerical study. An important use of the asymptotic theory is to help identify and elucidate the various energy-exchange mechanisms responsible for stabilization or destabilization of the instabilities. A reduction in the production of disturbance energy by the Reynolds shear stress is the main reason for the favourable effect of anisotropic wall compliance on instability growth. Other energy-exchange mechanisms, which have been found to make a significant contribution, include energy transfer from the disturbance to the mean flow due to the interaction of the fluctuating shear stress and the displaced mean flow, and the work done by the perturbations in wall pressure and shear stress.

It is found that anisotropic wall compliance confers very considerable advantage with respect to reduction in instability growth rate and transition delay. Using a fairly conservative criterion an almost ten-fold rise in transitional Reynolds number is predicted for anisotropic walls having the appropriate properties. Anisotropic wall compliance makes travelling-wave flutter much more sensitive to viscous effects and has a considerable stabilizing influence. The application of global convergence methods has led to the discovery of an anomalous spatially growing eigenmode which, according to conventional interpretation, would represent an instability. Further study of an appropriate initial-value problem has revealed that the new eigenmode is probably not an instability and that, for compliant walls, complex wavenumbers with positive real and negative imaginary parts do not necessarily correspond to an instability.

1. Introduction

The idea of reducing turbulence or instability growth rates by generating a negative Reynolds shear stress at the wall is likely to be appealing to most people

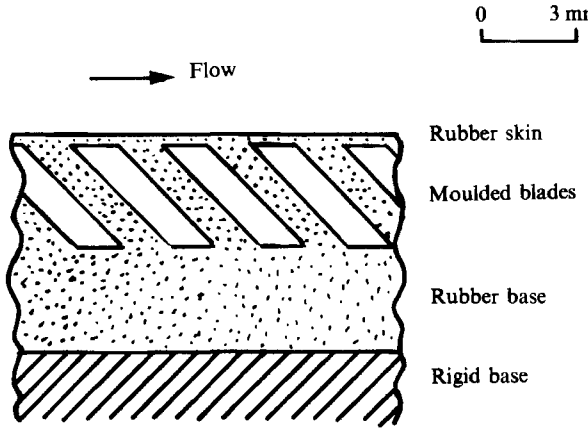

FIGURE 1. Cross-section of one of the non-isotropic compliant walls used by Grosskreutz (1971).

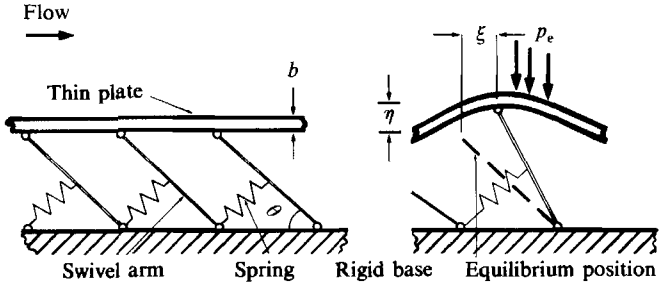

FIGURE 2. Schematic sketch of a simple surface-based theoretical model of an anisotropic compliant wall.

with a knowledge of fluid mechanics. Not surprisingly the concept has a fairly long history. It can be traced back at least as far as an unpublished report by Ffowcs Williams (1964). (The use of anisotropic wall compliance may even have originated with the dolphin (see §6.2).) The ideas used in the present paper stem from the work of Grosskreutz (1971, 1975). He carried out a series of experiments on turbulent flow over compliant walls of the type depicted in figure 1. The walls were made of silicone rubber and the inclined members were in the form of either blades or stalks. The basic idea behind the design of his walls was to ensure that, under the action of fluctuating pressure forces, the surfaces responded in such a way as to generate a negative Reynolds shear stress and thereby reduce the production of turbulence. Grosskreutz's experimental results were not particularly promising. Nonetheless, the basic idea remains attractive, not only for reducing turbulence levels but also for the postponement of laminar/turbulent transition. Accordingly, the theoretical model of the compliant wall, used for the present study and depicted in figure 2, is based, in part on a schematic sketch presented by Grosskreutz to explain his concept.

The theoretical model illustrated in figure 2 comprises a thin plate supported on inclined, sprung, lever arms. Under the action of small-amplitude pressure fluctuations the ends of the lever arms will move in such a way that the horizontal and vertical displacements are simply related, that is

$$\xi \cos\theta = \eta \sin\theta, \tag{1.1}$$

where θ defines the equilibrium position of the swivel arms (see figure 2). With the

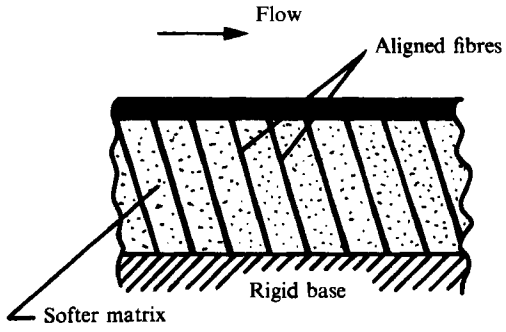

FIGURE 3. Sketch of a fibre-composite anisotropic compliant wall.

flow direction as shown in figure 2 the product of the streamwise and normal velocity components at the wall will always be positive, thereby giving a negative Reynolds shear stress.

What is meant by anisotropic wall compliance in the present context? We shall show in §2 that for the present model the speed of free waves is independent of direction. So at first sight the wall is not inherently anisotropic. When a fluid flows over the surface the symmetry of behaviour exhibited by waves to the left and right is broken. This in itself, though, does not constitute evidence for anisotropic wall compliance. For example, the simple plate/spring model, analysed by Carpenter & Garrad (1985, 1986), and the single- and two-layer compliant walls, investigated by Duncan, Waxman & Tulin (1985), Fraser & Carpenter (1985), Duncan (1988) and Yeo (1988), also exhibit a lack of symmetry between upstream- and downstream-travelling waves when interacting with a fluid flow. These compliant walls would not usually be considered anisotropic. The crucial distinction is that the response of the isotropic walls would remain invariant to flow direction, whereas in the present case the relationship (1.1) between the streamwise and normal surface displacements would undergo a change of sign when the flow direction is reversed. The analysis given in the present paper will show that this change of sign has important consequences. Thus in the present context, which is restricted to two-dimensional disturbances, the term anisotropic wall compliance connotes a change in response when the direction of flow is reversed, rather than an inherent anisotropy which would be revealed by the properties of free waves. When three-dimensional disturbances are considered, other types of anisotropic wall compliance become significant, for example orthotropic plates supported on springs, see Carpenter (1984*b*) and Joslin, Morris & Carpenter (1990). These will be analysed in subsequent papers.

Figure 2 could be regarded as depicting a theoretical model of the Grosskreutz surface illustrated in figure 1, in much the same way as the plate/spring model of Carpenter & Garrad was used to study the original Kramer (1960) coatings. Alternatively, just as the plate/spring model can be regarded as a rough approximation for the two-layer compliant walls used by Daniel, Gaster & Willis (1987) (see also Gaster 1987) in their experiments, the present model can be thought of as an approximate representation of the more practical anisotropic compliant wall depicted in figure 3. This wall comprises a thin plate covering an anisotropic fibre-composite substrate which consists of inclined stiff fibres imbedded in a soft viscoelastic matrix. The fibres would be so oriented as to lie in planes making an angle θ to the horizontal. Following this analogy θ will hereafter be referred to as the

fibre angle. The type of model illustrated in figure 2 was termed *surface-based* by Carpenter (1990) because the associated equation of motion does not depend on y, the coordinate perpendicular to the surface. It is possible to develop a more realistic *volume-based* theoretical model of such an anisotropic wall and this has been done by Yeo (1986, 1990). For his wall model the equations of motion for the wall depend on y with a consequent increase in the computational requirements and in the complexity of the problem. More general anisotropic compliant-wall models will be investigated analytically in the present study, but the numerical investigation will be confined to the relatively simple surface-based model. Its relative simplicity has great advantages for carrying out a comprehensive numerical study and for clarifying the role of the various stabilizing and destabilizing mechanisms which come into play when a fluid flow interacts with an anisotropic compliant wall.

The present paper represents the culmination of several years work on the effects of anisotropic wall compliance on boundary-layer stability and transition. Preliminary versions of various aspects of the work have appeared in conference proceedings and elsewhere. An analysis of the growth of Tollmien–Schlichting waves over the present compliant-wall model was presented by Carpenter (1984*c*). He found that the instability growth rates and the size of the unstable region in frequency/Reynolds-number space were both dramatically reduced as the fibre angle was increased. As expected it was found that reversing the flow direction led to a rise in instability growth rates. The initial indications were that this sort of surface had great potential for transition delay. This still remains the case.

An important feature of boundary-layer instability over compliant walls is the existence of several other modes, or types, of instability in addition to Tollmien–Schlichting waves. These were termed flow-induced surface instabilities by Carpenter & Garrad (1985) because unlike Tollmien–Schlichting waves they depend fundamentally on surface flexibility and could exist in an inviscid flow. They are similar to the instabilities encountered in aero- and hydroelasticity. Two main types of these flow-induced surface, or hydroelastic, instabilities are found in the case of the compliant wall illustrated in figure 2. These are: divergence, which occurs in the form of a stationary or very slowly moving wave; and, travelling-wave flutter, which typically has phase speeds close to the free-stream velocity. Carpenter & Garrad (1986) showed that divergence is an absolute instability, whereas, like Tollmien–Schlichting waves, travelling-wave flutter is a convective instability. But, whereas Tollmien–Schlichting waves belong to the Class A waves of Benjamin (1960, 1963) and Landahl (1962), travelling-wave flutter belongs to their Class B. This implies that the response of the travelling-wave flutter to irreversible energy transfer will be the exact opposite to that of the Tollmien–Schlichting waves. Consequently, as found by Carpenter & Garrad (1986), any wall property that has a stabilizing effect on the Tollmien–Schlichting waves will inevitably have a destabilizing effect on the travelling-wave flutter. It does not necessarily follow, therefore, that any real advantage will result from the use of anisotropic wall compliance. Stabilization of the Tollmien–Schlichting waves may be gained only at the expense of destabilizing travelling-wave flutter or divergence. Plainly it is essential to carry out a complete investigation, which properly takes into account the hydroelastic instability modes, before any firm conclusions can be drawn regarding the advantages or disadvantages of anisotropic wall compliance for transition control.

In order to take the hydroelastic instabilities into account properly an asymptotic theory for high Reynolds number was developed. This theory represents an extension of the relatively simple theory of Carpenter (1984*a*), and Carpenter &

Garrad (1986) for isotropic compliant walls. The new theory allows for horizontal, as well as vertical, wall displacements and also incorporates viscous effects. A preliminary version was presented by Carpenter (1985*a*) and it was found that, in contrast to the isotropic case, viscous effects, primarily in the form of fluctuating wall shear stresses, were highly significant for anisotropic compliant walls. Fortunately it was found that, although the original results of Carpenter (1984*c*) were somewhat optimistic, the use of anisotropic wall compliance could still lead to substantial reductions in the instability growth rates even with the hydroelastic instabilities properly taken into account. A more general and rigorous version of the asymptotic theory has been given by Carpenter & Gajjar (1990) and some preliminary results with the hydroelastic instabilities properly taken into account appeared in Carpenter & Morris (1985) and Carpenter (1987*b*). It has been found that the asymptotic theory also gives a reliable, albeit qualitative, guide to the effects of wall compliance on the Tollmien–Schlichting waves.

The formulation of the problem and the numerical methods used to solve it have also been developed and improved compared to those used initially. The original calculations by Carpenter (1984*c*, 1985*a*) were based on linear temporally growing instabilities and the formulation of the problem followed closely the methods of Carpenter & Garrad (1985). An improved formulation of the problem was given in Carpenter & Morris (1985) with a further improvement by Morris (1986). This is essentially the formulation followed in the present paper. The more realistic case of spatially growing linear instabilities was assumed by Carpenter & Morris and this is carried over to the present paper. In order to verify that all the potentially unstable modes were being taken into account, the globally convergent methods of Bridges & Morris (1984) were applied by Carpenter & Morris (1985) to the resulting eigenvalue problem. In this case the Orr-Sommerfeld equation was integrated numerically by means of a Chebyshev Tau spectral code. These methods are used in the present paper together with other numerical techniques.

One of the central problems of carrying out any numerical investigation of boundary-layer stability over a compliant wall is the proliferation of parameters relating to the wall properties. This problem is exacerbated by the introduction of anisotropic wall compliance which leads to a further increase in the number of wall parameters. One approach which greatly improves this state of affairs is to work with compliant walls having properties which render them marginally stable with respect to the two hydroelastic instabilities. This method was introduced by Carpenter (1985*b*, 1987*a*) for isotropic compliant walls. The original idea was that the surfaces with the best transition-delaying properties would need to be as compliant as possible without being vulnerable to hydroelastic instability. Thus, if the wall properties were restricted to the set that corresponded to marginal stability with respect to both divergence and travelling-wave flutter, the remaining wall parameter(s) could be varied to find the properties giving the greatest transition delay. This approach has considerable merit for application to the present case of anisotropic wall compliance. Apart from finding the wall properties which give the best performance in some specified sense, it also has two other advantages: it makes the amount of computing required more manageable and makes the comparison between walls with differing degrees of anisotropy more meaningful. The comparatively simple methods used to find these 'optimal' properties have recently been investigated by Joslin (1987) and Joslin & Morris (1989) who devised more rigorous numerical techniques for carrying out the optimization. They have been able to confirm that the relatively straightforward methods used in the present paper for

determining the 'optimal' properties give results which are reasonably close to the true optimum values. In the present paper we have also used the e^n method to predict transitional Reynolds numbers. This has allowed us to estimate the greatest transition delay possible using an anisotropic compliant wall. Adopting rather conservative criteria we estimate that a nearly ten-fold rise in transitional Reynolds number, as compared to the rigid surface, is possible in theory.

The work of Yeo (1986, 1990), using volume-based theoretical models of anisotropic compliant walls, was briefly mentioned above. This is a very thorough numerical investigation of the Tollmien–Schlichting and travelling-wave flutter (Class B) instabilities over various types of anisotropic compliant wall. It is an excellent piece of work and well worth studying in detail. Where appropriate Yeo's results will be compared to those obtained by means of the present methods, so detailed comments on his work are postponed until §6.3 and only a brief description given here. He considered two- and three-dimensional, spatially growing instabilities over various compliant walls. The two cases that are relevant to the present work are: (i) single-layer, fibre-composite walls with various fibre angles, elastic moduli and depths; (ii) double-layer walls, comprising a thin plate over a fibre-composite wall; again various combinations of properties were investigated. Our model may be regarded as an approximate model for the second case, but is less likely to be a good model for the first case. Yeo predicted transitional Reynolds numbers as high as 8.4 times the rigid-wall value for certain of the double-layer anisotropic compliant walls.

Before ending these introductory remarks it is worth commenting on one of Yeo's conclusions. He found that for anisotropic wall compliance with positive fibre angles the contribution of the negative Reynolds shear stress generated at the wall was virtually negligible. Accordingly, he concluded that the orientation of the fibres with respect to flow direction was unimportant. Our investigations substantially confirm Yeo's conclusions regarding the contribution of the negative Reynolds shear stress. But we find that for a compliant wall the boundary conditions at the surface exert an influence on the disturbance velocities that is felt across the whole boundary layer. This results in a substantial reduction in the Reynolds shear stress across most of the boundary layer, although there is a local rise in the vicinity of the viscous wall layer. Thus the production of energy by the Reynolds stress is reduced by wall compliance over the bulk of the boundary layer. This favourable effect is further enhanced for anisotropic compliant walls with positive fibre angle, but reduced when the fibre angle is negative. Thus the orientation of the fibres does have an important effect on energy production, but not primarily by the direct generation of negative Reynolds stress.

Furthermore, with our approach it is possible to study all the mechanisms responsible for irreversible energy exchange at the wall. We have found that, as well as energy production by the Reynolds stress and viscous dissipation, additional energy transfer between the disturbance and the mean flow due to the interaction of the fluctuating shear stress and the displaced mean flow, and the rate of irreversible work done by the fluctuating wall pressure and shear stress also play important roles in determining the response of the Tollmien–Schlichting waves to anisotropic wall compliance. These additional energy-transfer mechanisms are sensitive to the orientation of the fibres. Anisotropic wall compliance substantially changes the phase shift in the eigenfunction (normal velocity of disturbance) which occurs across the viscous wall layer. The change in phase is favourable for stabilization of the Tollmien–Schlichting waves when θ is positive, because it leads to a rise in the irreversible work done by the fluctuating wall pressure. The phase shift in the wall

layer also occurs for isotropic walls, as shown by Carpenter & Gajjar (1990), and is destabilizing in this case, but is outweighed by the phase shift of opposite sign which occurs across the critical layer. When the flow direction is reversed, i.e. θ is negative, the unfavourable phase shift across the wall layer, occurring in the isotropic case, is magnified. This reduces the irreversible work done by the fluctuating wall pressure, thereby destabilizing the Tollmien–Schlichting waves. Irreversible energy transfer at the wall due to the work done by the fluctuating shear stress also varies asymmetrically with θ, but in a rather more complex way. Thus, in contrast to Yeo, we conclude that the sign of θ is important, although the reasons are a good deal more complex than the initial simple physical arguments based on the sign of the Reynolds shear stress would suggest. We do agree with Yeo, however, with respect to the indifference of the hydroelastic instabilities to the sign of the fibre angle.

The remainder of the present paper is set out as follows. The theoretical model for the anisotropic compliant wall is described in §2 where the equation of motion is derived and the properties of the free waves are investigated. The formulation of the eigenvalue problem, corresponding to the coupled Orr–Sommerfeld and wall equations, is discussed in §3. The numerical methods are discussed in §4. Section 5 is devoted to the asymptotic theory for high Reynolds numbers and its implications and applications. This section contains the most fundamental results and much of the analysis and results apply to general anisotropic and isotropic compliant walls, including those of Yeo. It is made up of the following sub-sections. The asymptotic theory is described briefly in §5.1. The concept of inviscid equivalence between isotropic and anisotropic compliant walls for the hydroelastic instabilities is developed in §5.2. In §5.3 the concept of optimal wall properties is developed. The mechanisms for stabilization and destabilization are studied in §5.4, both by means of energy equations for the flow and the wall, and by means of the asymptotic theory. Finally in §5.5 the asymptotic theory is used to investigate the effect of anisotropic wall compliance on the travelling-wave-flutter instability. The results of the numerical investigation of instability and transition delay are presented in §6. The results obtained by using a global convergence scheme are described in §6.1. Perhaps the most significant outcome of this part of the numerical investigation was the discovery of an anomalous, apparently unstable, spatially growing eigenmode for which the real part of the complex wavenumber is positive and the imaginary part negative. Notwithstanding the conventional interpretation, the eigenmode probably does not represent an instability. The main results for boundary-layer stability and transition delay are presented in §6.2. A brief comparison between the present study and that of Yeo (1986, 1988, 1990) is made in §6.3. Finally §7 contains the main conclusions of the investigation.

2. Theoretical model for anisotropic compliant wall

For the present study the compliant surface is permitted to move in both the horizontal and vertical directions. In general, for such cases two equations of motion would be required. Considerable simplification can be achieved by adopting the surface-based theoretical model illustrated in figure 2. This model retains the essential features of anisotropic wall compliance but has the advantage that there is a simple relationship (1.1) between the horizontal and vertical displacements. The more general case will be considered in §5. The model can be thought of as an approximate representation of a compliant wall comprising a thin plate supported on an anisotropic substrate which consists of sheets of relatively stiff fibres embedded

in a softer matrix, see figure 3. As a consequence of the relationship (1.1) between the horizontal and vertical displacements only one equation of motion is required for such a compliant wall.

Since only small displacements of the surface are being considered the principle of superposition can be used to determine the restorative structural forces generated by the hydrodynamic driving forces. First, consider the forces per unit area perpendicular to the surface. In this case the driving force is $-(p'_{\rm w}-\sigma'_{\rm w})$ where $p'_{\rm w}$ and $\sigma'_{\rm w}$ are respectively the fluctuating dynamic pressure and direct viscous stress. In general the effects of a perturbation in body force should also be included and this is given by $g(\rho-\rho_{\rm s})$ where g is the acceleration due to gravity, ρ is the density of the free stream and $\rho_{\rm s}$ is the density of the substrate, whether solid or fluid. Classic thin-plate theory can be used, as in Carpenter & Garrad (1985, 1986), to give the corresponding opposing force due to the bending stiffness in the form $B\partial^4\eta/\partial x^4$, where B is the flexural rigidity given by

$$B = \frac{Eb^3}{12(1-\nu_{\rm P}^2)} \tag{2.1}$$

where E is the elastic modulus of the plate material, b is the plate thickness, and $\nu_{\rm P}$ is the Poisson ratio. In addition to this there is the vertical component of the spring force given by $Kl\delta\theta\cos\theta = K\eta$ where K is the spring stiffness, l is the length of the swivel arms (fibres), and $\delta\theta$ is the angular displacement of the end of a swivel arm from its equilibrium position.

The driving force per unit area horizontal to the surface is supplied by the fluctuating shear stress, $\tau'_{\rm w}$. It is opposed by the horizontal component of the spring force, $Kl\delta\theta\sin\theta = K\xi$. In addition there is a tension force per unit area induced in the plate by differential motion of the swivel arms.

In order to derive an expression for the induced tension per unit area let us consider three adjacent swivel arms. Let the equilibrium positions of their ends be given by $x-\delta x, x, x+\delta x$. The respective horizontal displacements would be

$$\xi-\frac{\partial\xi}{\partial x}\delta x+\frac{1}{2}\frac{\partial^2\xi}{\partial x^2}(\delta x)^2, \quad \xi, \quad \xi+\frac{\partial\xi}{\partial x}\delta x+\frac{1}{2}\frac{\partial^2\xi}{\partial x^2}(\delta x)^2.$$

Thus the strains in each of the portions of plate either side of the central swivel arm are given by

$$1+\frac{\partial\xi}{\partial x}-\frac{1}{2}\frac{\partial^2\xi}{\partial x^2}\delta x \quad \text{and} \quad 1+\frac{\partial\xi}{\partial x}+\frac{1}{2}\frac{\partial^2\xi}{\partial x^2}\delta x.$$

From the values of the strains and from the application of Hooke's law the net horizontal tension force acting on the central swivel arm can be obtained in the form $Eb(\partial^2\xi/\partial x^2)\,\delta x$. Provided that the swivel arms (or fibre sheets) are sufficiently close together compared to the wavelength of the instability, the limit $\delta x\to {\rm d}x$ can be taken.

For small displacements a point on the surface can be thought of as moving in one direction only, i.e. perpendicular to the equilibrium position of the swivel arms (fibres) – as suggested in figure 2. If the vertical and horizontal forces per unit area given above are resolved in this direction a single equation of motion can be written as

$$\rho_{\rm m} b\frac{\partial^2(l\delta\theta)}{\partial t^2} = -(p'_{\rm w}-\sigma'_{\rm w})\cos\theta+\tau'_{\rm w}\sin\theta-K_{\rm E}\,l\delta\theta+Eb\frac{\partial^2\xi}{\partial x^2}\sin\theta-B\frac{\partial^4\eta}{\partial x^4}\cos\theta, \tag{2.2}$$

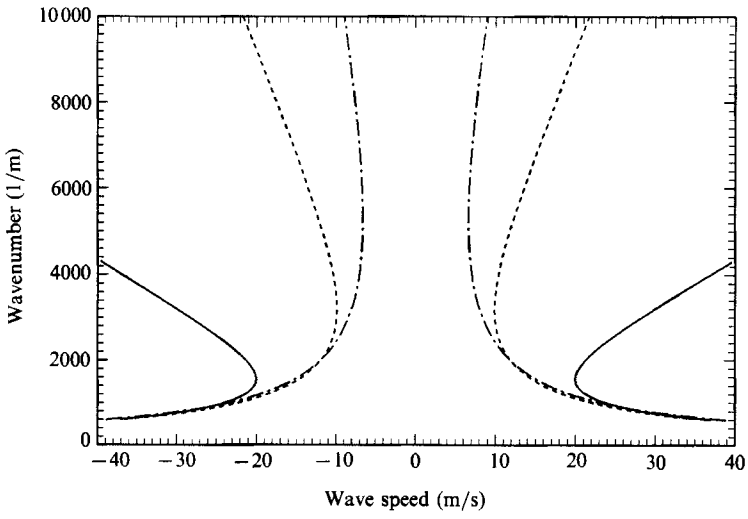

FIGURE 4. Dispersion curves for free waves over anisotropic compliant walls. The properties are as in figure 18 with material density equal to 1000 kg/m^3 and Poisson ratio 0.5. ——, $\theta = 0$; – – –, $\theta = 45°$; —·—, $\theta = 60°$.

where ρ_m is the density of the plate material and the equivalent spring stiffness, K_E, incorporates the perturbations in body force and is defined by

$$K_E = K - g(\rho - \rho_s)\cos\theta. \tag{2.3}$$

The term on the left-hand side of (2.2) represents the mass per unit area of the plate times its acceleration. The terms on the right-hand side of (2.2) represent the various forces per unit area acting on the plate. The first two of these are the driving hydrodynamic forces generated by the disturbances in the boundary layer and the remainder are the various restorative structural forces in the compliant wall.

When (1.1) is substituted, noting that $\eta_t \equiv l\delta\theta = \eta/\cos\theta$, (2.2) can be rewritten solely in terms of η_t as

$$b\rho_m \frac{\partial^2\eta_t}{\partial t^2} + B\cos^2\theta \frac{\partial^4\eta_t}{\partial x^4} - Eb\frac{\partial^2\eta_t}{\partial x^2}\sin^2\theta + K_E\eta_t = (-p'_w + \sigma'_w)\cos\theta + \tau'_w\sin\theta. \tag{2.4}$$

Material damping could be incorporated into the model in the same way as by Carpenter & Garrad (1985). They used a complex elastic modulus to model the viscoelastic properties of the materials. This approach can be carried over to the present case by introducing a complex elastic modulus for the plate material and/or a complex spring stiffness to model the viscoelastic properties of the substrate material. The viscoelastic loss factor is the ratio of the imaginary to the real part of the elastic modulus or spring stiffness.

Let us now consider briefly the behaviour of free waves for the present model. Assume that the surface displacement takes the form of a travelling wave, so that $\eta \sim \exp[i\alpha(x-ct)]$, where α is the wavenumber and c is the phase speed. When the fluctuating pressure and viscous stress terms in (2.4) are set equal to zero,

substitution of the above wave form in (2.4) yields a simple quadratic equation for c which can be solved to give

$$c_0^2 = \frac{\alpha^4 B\cos^2\theta + \alpha^2 Eb\sin^2\theta + K_E}{\alpha^2 b\rho_m}. \tag{2.5}$$

The notation c_0 has been introduced to indicate that this is the free-wave speed.

Note that, as mentioned in §1, (2.5) is invariant with respect to $\operatorname{sgn}\theta$ and, accordingly, c_0 is the same for left- and right-running waves. In this sense the model is not inherently anisotropic. It does, however, respond in an anisotropic manner to flow-generated forces, in the sense that the response changes when the flow direction is reversed. Typical variations of c_0 with wavenumber are shown in figure 4. The minimum that occurs in the variation of free-wave speed with wavenumber is an important feature for deriving simple formulae for predicting the onset speeds of the hydroelastic instability modes. When θ is set equal to zero, (2.2) and (2.5) reduce to the forms given by Carpenter & Garrad (1985, 1986) for the isotropic case.

3. Formulation of the problem

The fundamental problem considered here is the development of two-dimensional disturbances in a two-dimensional boundary layer flowing over a deformable surface. It is assumed that the boundary layer is locally parallel and that the disturbance velocity is sufficiently small for linear theory to hold.

The two perturbation velocity components and pressure are expressed in the form:

$$\{u', v', p'\} = \{U_\infty \hat{u}, U_\infty \hat{v}, \rho U_\infty^2 \hat{p}\}E + \text{c.c.}, \tag{3.1}$$

where $E = \exp\{\mathrm{i}(\alpha x - \omega t)\}$, U_∞ is the free-stream speed, and u' and v' are respectively the streamwise and normal disturbance velocities. Here we are considering spatially growing disturbances so $\alpha\,(=\alpha_r+\mathrm{i}\alpha_i)$ is the complex wavenumber and ω is the real frequency of the disturbance. α_r and $-\alpha_i$ are respectively the physical wavenumber and growth rate of the disturbance. The complex phase speed is given by $c = \omega/\alpha$; but ω/α_r corresponds to the actual phase speed.

When (3.1) is substituted into the linearized Navier–Stokes equations, which are then made non-dimensional in the conventional way, the following three equations are obtained for $\hat{u}$, $\hat{v}$,and $\hat{p}$:

$$-\mathrm{i}(\bar{\omega}^* - \bar{\alpha}^*\bar{U})\,\hat{u} + \mathrm{D}\bar{U}\hat{v} + \mathrm{i}\bar{\alpha}^*\hat{p} - \frac{1}{Re}(\mathrm{D}^2 - \bar{\alpha}^{*2})\,\bar{U} = 0, \tag{3.2}$$

$$-\mathrm{i}(\bar{\omega}^* - \bar{\alpha}^*\bar{U})\,\hat{v} + \mathrm{D}\hat{p} - \frac{1}{Re}(\mathrm{D}^2 - \bar{\alpha}^{*2})\,\hat{v} = 0, \tag{3.3}$$

$$\mathrm{i}\bar{\alpha}^*\hat{u} + \mathrm{D}\hat{v} = 0, \tag{3.4}$$

where $D \equiv \mathrm{d}/\mathrm{d}\bar{y}$, $Re \equiv U_\infty \delta^*/\nu$, δ^* is the boundary-layer displacement thickness, ν is the free-stream kinematic viscosity, and overbars denote non-dimensionalization with respect to δ^* or U_∞ as appropriate. The asterisks are used to distinguish between non-dimensionalization using δ^* as the reference length and the use of U_∞/ν later in the paper.

$\hat{p}$ and $\hat{u}$ can be eliminated from (3.2)–(3.4) to obtain the Orr–Sommerfeld equation in terms of $\hat{v}$, i.e.

$$\left[\left(\bar{U} - \frac{\bar{\omega}^*}{\bar{\alpha}^*}\right)(\mathrm{D}^2 - \bar{\alpha}^{*2}) - \mathrm{D}^2\bar{U}\right]\hat{v} = -\frac{\mathrm{i}}{\bar{\alpha}^* Re}(\mathrm{D}^2 - \bar{\alpha}^{*2})^2\,\hat{v}. \tag{3.5}$$

The usual outer boundary conditions are imposed on $\hat{u}$ and $\hat{v}$ requiring them to decay exponentially as $\bar{y} \to \infty$. At the wall the velocity is required to be continuous across the deformable surface. The surface displacements are expressed in the form:

$$\{\xi, \eta\} = \{\hat{\xi}^*, \hat{\eta}^*\}\delta^* E + \text{c.c.} \tag{3.6}$$

The linearized boundary conditions at the surface then become

$$\hat{u}_w = -\mathrm{i}\bar{\omega}^*\hat{\xi}^* - \hat{\eta}^* \mathrm{D}\bar{U}_w, \tag{3.7}$$

$$\hat{v}_w = -\mathrm{i}\bar{\omega}^*\hat{\eta}^*, \tag{3.8}$$

where suffix w denotes evaluation at the wall, i.e. at $\bar{y} = 0$, and $\mathrm{D}\bar{U}_w$ is the non-dimensional undisturbed velocity gradient at the wall. Equations (3.7) and (3.8) are a straightforward extension of the boundary conditions originally derived by Benjamin (1960) and Landahl (1962) (see also Carpenter & Garrad 1985).

Using the continuity equation (3.4), (3.8) and (1.1), the boundary condition (3.7) can be re-expressed solely in terms of $\hat{v}_w$ and its derivatives as

$$\bar{\omega}^* \cos\theta \mathrm{D}\hat{v}_w + (\cos\theta \mathrm{D}\bar{U}_w + \mathrm{i}\bar{\omega}^* \sin\theta)\,\bar{\alpha}^*\hat{v}_w = 0. \tag{3.9}$$

Using (2.5) the non-dimensional free-wave speed can be expressed as

$$\bar{c}_0 = \frac{c_0}{U_\infty} = \left(\frac{\bar{\alpha}^{*4} C_B^* \cos^2\theta + \bar{\alpha}^{*2} C_T^* \sin^2\theta + C_{KE}^*}{C_M^* \bar{\alpha}^{*2}}\right)^{\frac{1}{2}}, \tag{3.10}$$

where the non-dimensional wall parameters are defined as follows

$$C_M^* = \frac{b\rho_m}{\rho\delta^*}, \quad C_B^* = \frac{B}{\rho U_\infty^2 \delta^{*3}}, \quad C_T^* = \frac{Eb}{\rho U_\infty^2 \delta^*}, \quad C_{K_E}^* = \frac{K_E \delta^*}{\rho U_\infty^2}. \tag{3.11}$$

Using (3.10) and (3.11) the equation of motion (2.4) for the wall can be expressed in non-dimensional terms as

$$C_M^*(\bar{\omega}^{*2} - \bar{\alpha}^{*2}\bar{c}_0^2) + \mathrm{i}\bar{\omega}^* \cos^2\theta \frac{\hat{p}_w - \hat{\sigma}_w - \hat{\tau}_w \tan\theta}{\hat{v}_w} = 0, \tag{3.12}$$

where the non-dimensional amplitudes, $\hat{\sigma}_w$ and $\hat{\tau}_w$, of the viscous stresses are defined similarly to $\hat{p}$.

In order to express the equation of motion in terms of $\hat{v}$ and its derivatives expressions have to be derived for $\hat{p}_w$, $\hat{\sigma}_w$ and $\hat{\tau}_w$. The expression for pressure can be obtained from (3.2) with use of (3.4) to eliminate $\hat{u}$. It takes the form:

$$\hat{p}_w = \frac{1}{Re\,\bar{\alpha}^{*2}}(\mathrm{D}^3\hat{v}_w - \bar{\alpha}^{*2}\mathrm{D}\hat{v}_w + \bar{\alpha}^*\bar{\omega}^* Re\,\hat{v}_w \tan\theta). \tag{3.13}$$

The expressions for the two viscous stresses can be derived from Newton's law of viscosity with use of (3.4) to eliminate $\hat{u}$. Thus we obtain

$$\hat{\sigma}_w = \frac{2}{Re}\mathrm{D}\hat{v}_w, \quad \hat{\tau}_w = \frac{\mathrm{i}}{\bar{\alpha}^* Re}(\mathrm{D}^2\hat{v}_w + \bar{\alpha}^{*2}\hat{v}_w). \tag{3.14}$$

In order to obtain the equation of motion (3.12) in the final version used for the present work we substitute (3.11), (3.13) and (3.14), multiply by $\bar{\omega}^*/C_M^*$, and then

substitute for $\bar{\alpha}^* \hat{v}_w$ in terms of $D\hat{v}_w$ from a slightly rearranged version of (3.9). This gives

$$\left[\frac{C_B^*}{C_M^*}\cos^2\theta D\hat{v}_w\right]\bar{\alpha}^{*5}+\left[\frac{C_T^*}{C_M^*}\sin^2\theta D\hat{v}_w\right]\bar{\alpha}^{*3}+\left[(2\bar{\omega}^*\sin\theta-3iD\bar{U}_w\cos\theta)\frac{\cos\theta}{C_M^* Re}D\hat{v}_w\right]\bar{\alpha}^{*2}$$
$$+\left[\left(\frac{C_{KE}^*}{C_M^*}-\bar{\omega}^{*2}\right)D\hat{v}_w+(\cos\theta D\bar{U}_w+i\bar{\omega}^*\sin\theta)\frac{\sin\theta}{C_M^* Re}D^2 v_w\right]\bar{\alpha}^*$$
$$+\left[i(\cos\theta D\bar{U}_w+i\bar{\omega}^*\sin\theta)\frac{\cos\theta}{C_M^* Re}D^3\hat{v}_w-i\frac{\bar{\omega}^{*2}}{C_M^*}\sin\theta\cos\theta D\hat{v}_w\right]=0. \quad (3.15)$$

The Orr–Sommerfeld equation (3.5) together with the usual outer boundary conditions and the wall boundary conditions (3.9) and (3.15) define the appropriate eigenvalue problem; $\bar{\alpha}^*$ is the complex eigenvalue and $\hat{v}$ the eigenfunction. Although (3.7) has been used in the derivation of (3.15) and (3.9) it is not imposed explicitly because for the linear problem the amplitude of the wall motion is arbitrary.

4. Numerical Methods

4.1. *Integration of the Orr–Sommerfeld equation using a shooting method*

In order to perform e^n-type calculations a considerable amount of computing is required. This made it highly desirable to have an efficient code for the numerical integration of the Orr–Sommerfeld equation (3.5). For this reason the shooting method described below was developed, despite our having access to computer codes based on other methods (see §4.3).

The Orr–Sommerfeld equation (3.5) is recast as a system of four first-order ordinary differential equations for the complex eigenvector

$$\boldsymbol{V}=[\hat{v}, D\hat{v}, D^2\hat{v}, D^3\hat{v}]^T. \quad (4.1)$$

In a similar way the wall boundary conditions (3.9) and (3.15) can be rewritten in the form:

$$\boldsymbol{A}\boldsymbol{V}=0 \quad (4.2)$$

where $\boldsymbol{A}$ is a 2×4 matrix with the elements A_{13}, A_{14} and A_{21} equal to zero and the remaining elements non-zero.

There are four fundamental solutions, $\boldsymbol{V}_i (i=1,\ldots,4)$, to (3.5), so its general solution may be written in the form $\boldsymbol{V}=C_i\boldsymbol{V}_i$ where repeated suffices imply summation from $i=1$ to 4. At the wall we take $\boldsymbol{V}_1=[1,0,0,0]^T$, $\boldsymbol{V}_2=[0,1,0,0]^T$ etc. However, two of the constants of integration, say C_1 and C_2, can be eliminated by using the wall boundary conditions (4.2), ((3.9) and (3.15)). In this way two linearly independent starting solutions can be derived which satisfy the wall boundary conditions and take the forms

$$\left.\begin{aligned}\tilde{\boldsymbol{V}}_1&=\left[\frac{A_{12}A_{23}}{A_{22}A_{11}},-\frac{A_{23}}{A_{22}},1,0\right]^T,\\ \tilde{\boldsymbol{V}}_2&=\left[\frac{A_{12}A_{24}}{A_{22}A_{11}},-\frac{A_{24}}{A_{22}},0,1\right]^T.\end{aligned}\right\} \quad (4.3)$$

This procedure is similar to that used by Yeo (1986, 1988).

With the starting solutions specified by (4.3) the Orr–Sommerfeld equation (3.5) is integrated numerically across the boundary layer by using a fixed-step fourth-order Runge–Kutta method. The linear independence of $\tilde{\boldsymbol{V}}_1$ and $\tilde{\boldsymbol{V}}_2$ is preserved by

using Gram–Schmidt ortho-normalization when necessary (see Bellman & Kalaba 1965).

Beyond the edge of the boundary layer, here taken as $\bar{y} = \bar{y}_e \approx 8$, two ortho-normal fundamental solutions, $\tilde{V}_3$ and $\tilde{V}_4$ may be constructed from the usual forms of the two exponentially decaying fundamental solutions in the free stream, namely

$$\exp(-|\bar{\alpha}^*|\,\bar{y}) \quad \text{and} \quad \exp(-[\bar{\alpha}^{*2} + iRe\,(\bar{\alpha}^* - \bar{\omega}^*)]^{\frac{1}{2}}\bar{y}).$$

If the correct choice of eigenvalue has been made then the numerically constructed solution at the edge of the boundary layer will match the free-stream solution so that

$$\tilde{C}_1\,\tilde{V}_1(\bar{y}_e) + \tilde{C}_2\,\tilde{V}_2(\bar{y}_e) = -\tilde{C}_3\,\tilde{V}_3(\bar{y}_e) - \tilde{C}_4\,\tilde{V}_4(\bar{y}_e), \tag{4.4}$$

where the $\tilde{C}_i$ are constants of integration. Note that the arbitrary choice of sign for $-\tilde{C}_3$ and $-\tilde{C}_4$ is made for convenience in the definition of $\boldsymbol{M}$ below.

In order to obtain a non-trivial solution for $\tilde{\boldsymbol{C}} = [\tilde{C}_1, \ldots, \tilde{C}_4]$, thereby indicating that the correct choice has been made for $\bar{\alpha}^*$, we require that

$$\det(\boldsymbol{M}) = 0 \tag{4.5}$$

where $\boldsymbol{M} = [\tilde{V}_1(\bar{y}_e), \tilde{V}_2(\bar{y}_e), \tilde{V}_3(\bar{y}_e), \tilde{V}_4(\bar{y}_e)]^{\mathrm{T}}$.

As in Carpenter & Garrad (1985), the method of false position is used as the iterative method for determining the value of $\bar{\alpha}^*$ satisfying (4.5).

The advantage of initiating the shooting scheme at the wall, rather than at the edge of the boundary layer, as is more common, is that it allows the Blasius equation to be integrated numerically along with the Orr–Sommerfeld equation using the same Runge–Kutta scheme.

4.2. *The* e^n*-type computations*

These computations are based on the e^n-method of transtion prediction developed originally by Smith & Gamberoni (1956), (see also Jaffe, Okamura & Smith 1970). The computations are initiated by choosing a non-dimensional frequency,

$$F = \frac{\omega\nu}{U_\infty^2} \times 10^6 = \frac{\bar{\omega}^*}{Re} \times 10^6, \tag{4.6}$$

and an initial value of Re just below that corresponding to the lower branch of the neutral curve at the chosen frequency. The computations advance in steps of Re equal to 50 until the upper branch of the neutral curve has been crossed. At each value of Re the shooting method together with the method of false position, as described above, is used to determine the complex eigenvalue $\bar{\alpha}^*$. Cubic splines are then fitted to the data pairs $(Re, -\alpha_i^*)$ to obtain an interpolation function. The secant method is used to determine the two neutral points from this interpolation function.

The total amplification rate at a given streamwise position, x, (or corresponding Reynolds number) of the Tollmien–Schlichting wave having the specified frequency is given by

$$\frac{\hat{v}_x}{\hat{v}_i} = \exp\left[-\int_{x_i}^{x} \alpha_i \,\mathrm{d}x\right] = \exp\left[-\frac{2}{(1.7204)^2}\int_{Re_i}^{Re} \bar{\alpha}_i^* \,\mathrm{d}Re\right] \tag{4.7}$$

where suffix i denotes the values on the lower branch of the neutral curve. Thus $\hat{v}_i$ denotes the *initial* amplitude of the disturbance while $\hat{v}_x$ denotes the value at the current value of x attained after amplification during the passage downstream of the Tollmien–Schlichting wave. The successive values of the integral in (4.7) as x (or

equivalently, Re) is increased step by step downstream are obtained by numerical quadrature. When the upper branch of the neutral curve has been passed a new value of frequency F is then chosen and the whole procedure repeated.

The numerical-quadrature procedure is based on the analytical integration of the cubic splines over each Reynolds number interval of 50. This procedure was tested on functions with known exact integrals. The test functions chosen had a similar shape, maximum value and range as typical $\bar{\alpha}_1^*$ versus Re data. With the chosen value of 50 for the step in Re it was found that the integral could be evaluated to within a relative error of 0.1 % for a range from $Re = 1400$ to 2900. At higher values of Reynolds number the relative error is reduced.

4.3. *The globally convergent scheme*

The shooting method described in §4.1 requires an initial guess for the eigenvalue. This is no great disadvantage in the case of the Tollmien–Schlichting instability mode for which it was usually possible to make a sufficiently informed guess for the first eigenvalue and use extrapolation thereafter. In the case of the travelling-wave-flutter instability it was usually necessary for the initial guess to be very close to the exact eigenvalue to obtain convergence. Again, though, this is not a problem because of the highly accurate approximate eigenvalues predicted by the asymptotic theory of Carpenter & Gajjar (1990) (see §§5.1 and 5.5). Thus the shooting method and/or the asymptotic theory are more than adequate for dealing with two of the instabilities, but there remains the anxiety that other unsuspected instability modes may exist with the unusual wall properties under investigation. It is for this reason that we have extended the globally convergent scheme of Bridges & Morris (1984) to the present case. Globally convergent schemes provide the complete eigenvalue spectrum, or a specified subset of it, without requiring an initial guess.

A spectral Chebyshev Tau method is used to discretize the Orr–Sommerfeld equation (3.5) and the four boundary conditions. The problem is recast in much the same way as in §4.1 except that the semi-infinite $\bar{y}$ domain is transformed to the finite domain $-1 \leqslant z \leqslant 1$ using the algebraic transformation

$$z = \frac{\bar{y}-2}{\bar{y}+2}. \tag{4.8}$$

Equation (3.5) is then integrated indefinitely four times with respect to z. The eigenfunction is approximated by a finite Chebyshev series:

$$\hat{v}(z) = \tfrac{1}{2}v_0 T_0 + \sum_{n=1}^{N-1} v_n T_n(z) \tag{4.9}$$

and the Blasius velocity profile $\bar{U}(z)$ is also expanded in a finite Chebyshev series. These series are then substituted into the indefinitely integrated version of (3.5) and the coefficients of each order of Chebyshev polynomial equated to zero. The four equations which contain the constants of integration, arising from the four-fold integration of (3.5), may be replaced by the four boundary conditions. The result is a matrix equation of the form:

$$\boldsymbol{D}_5 \boldsymbol{v}_N = 0, \tag{4.10}$$

where $\boldsymbol{D}_5$ is a $N \times N$ matrix of the form:

$$\boldsymbol{D}_5 = \sum_{i=0}^{5} \boldsymbol{C}_i \bar{\alpha}^{*5-i} \tag{4.11}$$

and $\boldsymbol{v}_N$ and $\boldsymbol{C}_i$ are N-dimensional vectors; the former made up of the coefficients v_i in (4.9).

Five is the highest power of the eigenvalue $\bar{\alpha}^*$ appearing in (4.11). This comes from the wall boundary condition (3.15). Thus it can be seen that the eigenvalue appears nonlinearly in the matrix discretization of the problem. Consequently standard algorithms cannot be applied directly. However, equation (4.10) may be transformed to an algebraic eigenvalue problem of order $5N$. Since the QR algorithm requires computational times of order $4m^3$, where m is the order of the linear problem, it is clear that such a transformation requires a significant increase in computing time. However, (4.10) may be factorized using the matrix equivalent of synthetic division. This leads to an algebraic eigenvalue problem of order N.

Since $\boldsymbol{C}_0$ is singular it is convenient to shift the eigenvalue such that

$$\lambda = \frac{1}{\bar{\alpha}^* - s}. \tag{4.12}$$

Now eigenvalues close to s become dominant. Equation (4.11) may now be written as

$$\boldsymbol{D}_5(\lambda) = \sum_{i=0}^{5} \tilde{\boldsymbol{C}}_i \lambda^{5-i} = \boldsymbol{Q}_4(\lambda)(\boldsymbol{I}\lambda - \boldsymbol{Y}) + \boldsymbol{D}_5(\boldsymbol{Y}). \tag{4.13}$$

$\boldsymbol{Q}_4(\lambda)$ is a lambda matrix of degree four and $\boldsymbol{Y}$ is the right solvent. This factorization is equivalent to solving the fifth-order matrix polynomial

$$\boldsymbol{D}_5(\boldsymbol{Y}) = \sum_{i=0}^{5} \tilde{\boldsymbol{C}}_i \boldsymbol{Y}^{5-i} = 0. \tag{4.14}$$

Bernoulli iteration may be used to find either the minimal or dominant solvent of (4.14), as described by Bridges & Morris (1984), but the convergence may be slow. Dennis, Traub & Weber (1978) give an improved algorithm for the solvents of matrix polynomials. The application of this scheme to problems in hydrodynamic stability is described in Morris (1986). In the present case it has been found computationally efficient to obtain first a rough approximation to the eigenvalue spectrum using the first Bernoulli iteration step, namely

$$\boldsymbol{Y} \approx -\tilde{\boldsymbol{C}}_0^{-1} \tilde{\boldsymbol{C}}_1. \tag{4.15}$$

A cubically convergent, local-iteration scheme may then be used to refine the accuracy of selected eigenvalues. The details are given in Bridges & Morris (1984) and Morris (1986).

In the present case the global schemes were used to check that the Tollmien–Schlichting, travelling-wave flutter and divergence instabilities were the only unstable discrete eigenmodes present. This has been confirmed by the calculations to be presented in §6.1. However, a previously unreported anomalous discrete eigenmode, which would be unstable according to conventional interpretation, was identified and elucidated. This demonstrates the value of the global schemes for tracing eigenvalues in new or complex problems.

4.4. *Checking numerical methods by comparison with previous results*

It is important to ensure that the numerical schemes are accurate and free from error. The question of accuracy is of more than academic interest here because, generally, in order to achieve comparable accuracy in the case of the compliant wall a considerably smaller step in $\bar{y}$ is required as compared to the rigid wall. This problem seems to be exacerbated by the introduction of anisotropic wall compliance. Thus in order to ensure that the results reflect the nature of the theoretical model

under study, rather than numerical inaccuracy, the various numerical schemes were carefully checked.

The eigenvalues for the rigid wall, computed using the shooting method with 200 steps, agree to five significant places with values supplied by M. Gaster (1988, private communication) at $Re = 1500$. Gaster's code employed the compound-matrix method together with a fixed-step Runge–Kutta scheme. He integrated over 500 steps out to a value of the Blasius coordinate equal to 10.0 ($\bar{y} \approx 9.67$). We took 200 steps out to 8.0. This agreement between quite different methods is clearly satisfactory. We also obtained exact agreement with Jordinson's (1970) coordinates for the neutral-stability curve. Finally, as a check on the e^n-type calculations we calculated the value of n corresponding to $Re = 2900$ and non-dimensional frequency $F = 28.5 \times 10^{-6}$. We obtained $n = 8.28$, in exact agreement with Yeo (1986) and close to the value of 8.3 obtained by Jaffe *et al.* (1970).

Plainly our rigid-wall computations have been tested satisfactorily. In the case of the compliant wall, especially the anisotropic one, it is not so easy to test the codes since there are few established results. Fortunately, we had several completely different methods at our disposal to check against one another. In addition to the shooting method we also had the spectral code used for the globally convergent scheme and the accurate asymptotic theory of Carpenter & Gajjar (1990). For a typical anisotropic compliant wall it was found that 500 steps were required with the shooting method to obtain an accuracy comparable to that obtained with 200 steps for the rigid wall. To obtain comparable accuracy with the spectral code, 65 to 70 Chebyshev polynomials were required. The reason why the compliant walls required this considerably greater number of steps is not completely clear. It probably reflects the nature of the boundary condition (3.15) which contains higher derivatives of the eigenfunction. These higher derivatives stem originally from the expressions (3.13) and (3.14) for the fluctuating wall pressure and shear stress respectively.

5. The asymptotic theory and its implications

5.1. *Asymptotic theory*

An asymptotic theory for the hydroelastic or 'inviscid' instability modes of a boundary layer over anisotropic compliant walls is presented in Carpenter & Gajjar (1990). This theory is based in part on the concepts of Miles (1957, 1959*a*, *b*, 1962) and Benjamin (1959, 1963). Here an outline of the theory is given. The two main hydroelastic modes, namely divergence and travelling-wave flutter, have their origins in the two branches of the free-wave modes shown in figure 4. Thus the hydroelastic modes are fundamentally instabilities in the wall. This fact is exploited by using the equation (3.12) for the wall motion as the eigenvalue equation. This can be done provided suitable expressions can be found for the forcing terms due to the unsteady fluid flow. The derivation of these expressions is briefly described below. It should be emphasized that this theory and the resulting expressions for fluctuating wall pressure and viscous stresses are perfectly general, in that they apply equally well to any type of compliant wall, including the isotropic and anisotropic cases studied by Yeo (1986, 1988, 1990) and others. Moreover much of the physical interpretation arising from the theory also applies qualitatively to the Tollmien–Schlichting instability (TSI).

Let the small parameter for the theory be defined by

$$\epsilon = \frac{1}{Re^{\frac{1}{2}}}. \tag{5.1}$$

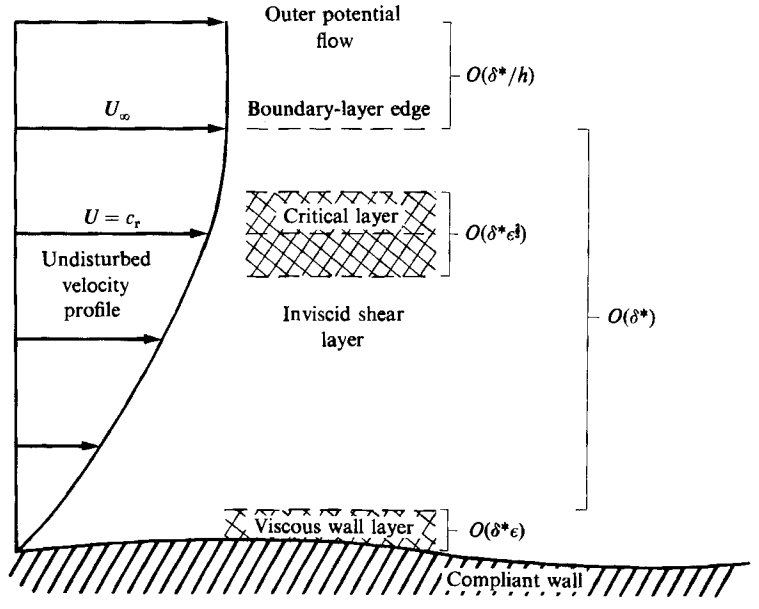

FIGURE 5. Schematic sketch of the multideck boundary-layer structure assumed for the asymptotic theory. δ_0^* is the boundary-layer displacement thickness at a fixed value of x, and h is a reference length of the same order of magnitude as the disturbance wavelength.

By rearranging the linearized y-momentum equation (3.3) and integrating with respect to $\bar{y}$ it can be shown that the amplitude of the fluctuating wall pressure is given by

$$\hat{p}_w = i\bar{\alpha}^* \int_0^\infty (\bar{U} - \bar{c})\, \hat{v}\, d\bar{y} + O(\epsilon^2). \tag{5.2}$$

Note that here it is convenient to use the phase speed $\bar{c} = \bar{\omega}^*/\bar{\alpha}^*$ as a parameter rather than $\bar{\omega}^*$.

In order to evaluate (5.2) and expressions (3.14) for the fluctuating viscous stresses at the wall, so that (3.12) may be used as an eigenvalue equation, asymptotic solutions of the linearized Navier–Stokes equations at high Reynolds number are required for $\hat{v}$. (To $O(\epsilon)$ the linearized Navier–Stokes equations are equivalent to the Orr–Sommerfeld equation (3.5).) These are obtained by exploiting the multideck structure of the boundary layer depicted in figure 5. It is assumed that the critical and wall layers, where viscous effects are important, are well separated. It is shown in Carpenter & Gajjar (1990) that the viscous effects in the critical layer do not affect the values of $\hat{p}_w$ or $\hat{\tau}_w$ to $O(\epsilon)$. Accordingly, viscous effects are ignored everywhere outside the wall layer. It is essential, however, that the phase jump across the critical layer be retained. Carpenter & Gajjar (1990) showed that an appropriate 'composite' asymptotic solution for $\hat{v}$, omitting the viscous effects in the critical layer, may be written as

$$\begin{aligned} \hat{v} &= C_1 \hat{v}_1 + C_2 \hat{v}_V \\ &= C_1 (\bar{U} - \bar{c})\, e^{-|\bar{\alpha}^*| y} (1 - |\bar{\alpha}^*|\, \Phi_1) + C_2 \exp(-e^{-\frac{1}{4}\pi i} \tilde{y}) + o(\epsilon), \end{aligned} \tag{5.3}$$

where C_1 and C_2 are constants of integration, $\tilde{y} = \bar{y}(\bar{\alpha}^* \bar{c})^{\frac{1}{3}}/\epsilon$, and

$$\Phi_1 \equiv \int_0^{\bar{y}} \left\{ \left(\frac{1 - \bar{c}_r}{\bar{U} - \bar{c}_r} \right)^2 - 1 \right\} d\bar{y}. \tag{5.4}$$

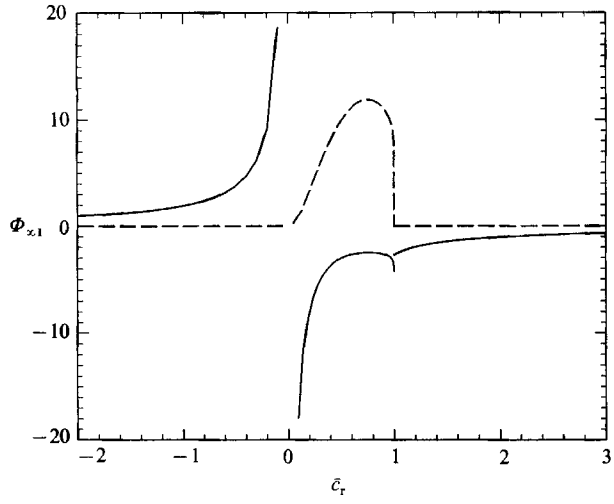

FIGURE 6. Variation of $\Phi_{\infty 1r}$ (——) and $\Phi_{\infty 1i}$ (– – – –) with $\bar{c}_r$.

The first term on the right-hand side of (5.3) is the inviscid part of the solution and is essentially the same as that given by Benjamin (1959, 1963). The second term represents the viscous correction for the wall layer. The constants of integration, C_1 and C_2, are evaluated by satisfying the boundary conditions (3.7) and (3.8) at the wall and are given by

$$C_1 = C_{10} + \epsilon C_{11}, \quad C_2 = \epsilon \bar{c} C_{11}, \tag{5.5}$$

where

$$C_{10} = \mathrm{i}\bar{\alpha}^* \hat{\eta}^*$$

and

$$C_{11} = \mathrm{i}\frac{\bar{\alpha}^{*2}}{(2\bar{\alpha}^*)^{\frac{1}{2}}}(1+\mathrm{i})\left[\frac{(1-\bar{c})^2}{\bar{c}^{\frac{5}{2}}}\right]\hat{\eta}^* + \frac{\bar{\alpha}^{*2}}{(2\bar{c}\bar{\alpha}^*)^{\frac{1}{2}}}(1+\mathrm{i})\,\hat{\xi}^*.$$

For the present two-dimensional case $\hat{u}$ may be readily derived from $\hat{v}$ using the continuity equation (3.4). See Carpenter & Gajjar (1990) for further details.

With C_1 and C_2 evaluated, (5.3) can be used to obtain the following expression for $\hat{p}_w$:

$$\hat{p}_w = -|\bar{\alpha}^*|(1-\bar{c})^2\hat{\eta}^* - \bar{\alpha}^{*2}\left\{2\bar{c} - 1 - \frac{1}{H} - (1-\bar{c})^2\Phi_{1\infty}\right\}\hat{\eta}^* - \frac{\epsilon\bar{\alpha}^{*2}}{(2\bar{c}\bar{\alpha}^*)^{\frac{1}{2}}}(1+\mathrm{i})(1-\bar{c})^2\left\{\frac{(1-\bar{c})^2}{\bar{c}^2}\hat{\eta}^* - \mathrm{i}\hat{\xi}^*\right\}, \tag{5.6}$$

where H is the ratio of the boundary-layer displacement thickness to momentum thickness (for the Blasius velocity profile $H = 2.591$), and where

$$\Phi_{1\infty} \equiv \int_0^\infty \left\{\left(\frac{1-\bar{c}_r}{\bar{U}-\bar{c}_r}\right)^2 - 1\right\}\mathrm{d}\bar{y}.$$

$\Phi_{1\infty}\,(= \Phi_{1\infty r} + \mathrm{i}\Phi_{1\infty i})$ is a complex quantity when $0 < \bar{c}_r < 1$, and in this case becomes a singular integral. It is evaluated by using a contour comprising the real $\bar{y}$-axis except for a semicircular indentation of infinitesimal radius under the critical point, $\bar{y}_c$ where $\bar{U} = \bar{c}_r$. The real and imaginary parts of $\Phi_{1\infty}$, $\Phi_{1\infty r}$ and $\Phi_{1\infty i}$ are plotted against $\bar{c}_r$ in figure 6.

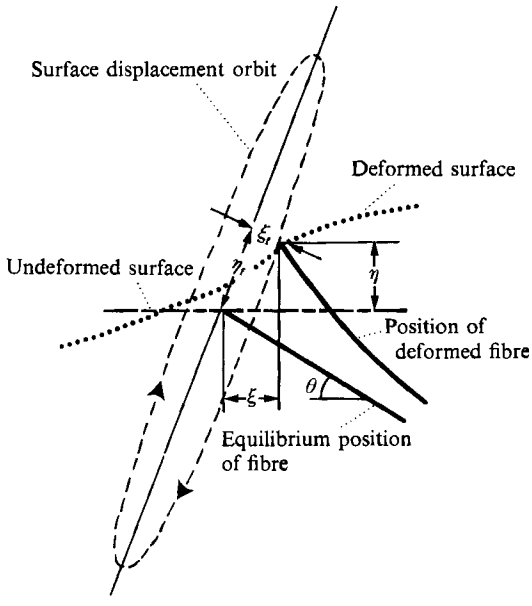

FIGURE 7. Schematic sketch showing the mode of surface deformation and defining notation for a more general fibre-composite anisotropic compliant wall.

The asymptotic solution (5.3) can also be used to obtain expressions from (3.14) for the fluctuating viscous stresses at the wall. These take the forms

$$\hat{\sigma}_w = 2\bar{\alpha}^* \epsilon^2 (-\bar{\alpha}^* \bar{c} \hat{\xi}^* + \mathrm{i} D \bar{U}_w \hat{\eta}^*), \tag{5.7}$$

$$\hat{\tau}_w = \frac{\epsilon \bar{c}^{\frac{3}{2}}}{\bar{\alpha}^{*\frac{1}{2}}} \left[\left(-\frac{1}{\sqrt{2}} + \frac{\mathrm{i}}{\sqrt{2}} \right) \frac{(1-\bar{c}^2)^2}{\bar{c}^2} \bar{\alpha}^{*2} \hat{\eta}^* + \left(\frac{1}{\sqrt{2}} + \frac{\mathrm{i}}{\sqrt{2}} \right) \bar{\alpha}^{*2} \hat{\xi}^* \right] + O(\epsilon^2). \tag{5.8}$$

From (5.7) it can be seen that $\hat{\sigma}_w$ is clearly a higher-order term and it is accordingly, dropped in what follows.

Interpolation functions describing $\Phi_{1\infty r}$ and $\Phi_{1\infty i}$ as functions of $\bar{c}_r$ are given in Carpenter & Gajjar (1990). When use is made of these, together with (5.5) and (5.8), the equation (3.12) of motion for the wall becomes a straightforward algebraic eigenvalue equation for $\bar{\alpha}^*$. This equation can be solved for $\bar{\alpha}^*$ by means of standard techniques at a minute fraction of the computing cost required for solutions of the full Orr–Sommerfeld equation. The results so obtained are found in Carpenter & Gajjar (1990) to be extremely accurate.

It is convenient for general applications to decompose the wall displacement into a component, ξ_f, parallel to the equilibrium position of the fibres and η_f perpendicular to the fibres. See figure 7. Note that $\xi_f$would be identically zero for the theoretical model described in §2 and figure 2. However, for more general models of the type of fibre-composite anisotropic wall illustrated in figure 3 and studied by Yeo (1986, 1990), both ξ_f and η_f would generally be non-zero. Yeo presents figures showing displacement orbits like that depicted in figure 7 and it is clear from these that the phase of ξ_f lags that of η_f by a factor of $\frac{1}{2}\pi$, so that

$$\xi_f = -\mathrm{i} f \eta_f,$$

where f is a positive real number. Note that the actual value of f can only be determined from a full solution to the coupled flow/wall problem.

The vertical and horizontal wall displacements are related to ξ_f and η_f as follows:

$$\hat{\eta}^* = \hat{\eta}_f^* \cos\theta - \hat{\xi}_f^* \sin\theta = \hat{\eta}_f^*(\cos\theta + \mathrm{i}f\sin\theta),$$
$$\hat{\xi}^* = \hat{\eta}_f^* \sin\theta + \hat{\xi}_f^* \cos\theta = \hat{\eta}_f^*(\sin\theta - \mathrm{i}f\cos\theta),$$

where the form and non-dimensionalization assumed for ξ_f and η_f are similar to those for ξ and η.

Usually it can be assumed that $f \ll 1$ so that

$$\frac{\hat{\xi}^*}{\hat{\eta}^*} = \frac{(1-f^2)\sin\theta\cos\theta - \mathrm{i}f}{\cos^2\theta + f^2\sin^2\theta} \approx \tan\theta - \frac{\mathrm{i}f}{\cos^2\theta}. \tag{5.9}$$

This is not an essential simplification in what follows but aids physical interpretation. The theoretical model of §2 and figure 2 corresponds to $f = 0$. In all the cases studied by Yeo (1986, 1990) $f \ll 1$. The stiffer the fibres compared to the softer matrix the smaller is f.

5.2. *Inviscid equivalence between anisotropic and isotropic compliant walls*

There are two main types of hydroelastic, or flow-induced, surface instabilities, namely *divergence* and *travelling-wave flutter* (TWF). In both cases the primary mechanism of destabilization is essentially inviscid. Viscous effects are thought to be insignificant for divergence but this still remains to be established properly. As shown in §5.4 and by the results presented in §5.5, viscous effects are not insignificant for TWF. Even so they come into play at higher order. Accordingly it is worthwhile to see if it is possible to make any general statements about the behaviour of these instabilities over anisotropic walls in the absence of viscosity.

When viscosity is ignored the two viscous-stress terms, $\hat{\sigma}_w$ and $\hat{\tau}_w$, in (3.12) are both zero. Also the expression (5.6) for the wall pressure, $\hat{p}_w$, becomes identical for both anisotropic and isotropic compliant walls. It follows, therefore, with use of the expression (2.5) for the free-wave speed, that in the absence of viscosity the equation of motion (3.12) for the anisotropic wall will be identical to that for an isostropic wall having the properties

$$B_E = B, \quad T_E = Eb\tan^2\theta, \quad K_{EE} = K_E/\cos^2\theta, \quad b_E = b\cos^2\theta, \tag{5.10}$$

where suffix E has been used to denote the property of the equivalent isotropic wall. It has been assumed in deriving (5.10) that the material density, ρ_m is the same in both cases. It is also assumed that the flow properties remain unchanged.

The equivalent properties given by (5.10) can be used to extend the results derived in Garrad & Carpenter (1982), Carpenter & Garrad (1986) and Yeo & Dowling (1987) to anisotropic compliant walls. Thus for the onset of divergence the critical wavenumber and flow speed are found by substituting (5.10) into equations (2.10) and (2.11) of Carpenter & Garrad (1986) and are given by

$$\alpha_d = \left[\frac{(T_E^2 + 12B_E K_{EE})^{\frac{1}{2}} - T_E}{6B_E}\right]^{\frac{1}{2}}$$
$$= \left[\frac{[(Eb\tan^2\theta)^2 + 12BK_E/\cos^2\theta]^{\frac{1}{2}} - Eb\tan^2\theta}{6B}\right]^{\frac{1}{2}}, \tag{5.11a}$$

$$U_d = c_0\left(\frac{b\rho_m\alpha_d}{\rho_e\cos^2\theta}\right)^{\frac{1}{2}}. \tag{5.11b}$$

Similarly, equations (3.6) and (3.7) of Carpenter & Garrad (1986) for the TWF over a non-dissipative compliant wall can be extended to the anisotropic case to read

$$\alpha_{cB} = \left(\frac{K_E}{B\cos^2\theta}\right)^{\frac{1}{4}}, \tag{5.12a}$$

$$U_{cB} = \left[\frac{2(BK_E/\cos^2\theta)^{\frac{1}{2}} + Eb\tan^2\theta}{b\rho_m\cos^2\theta}\right]^{\frac{1}{2}}. \tag{5.12b}$$

Equations (5.11) and (5.12) are used to derive optimal wall properties in the next section. The results presented in §5.5 suggest that (5.12) is rather conservative for anisotropic walls; but it will always hold in the limit $Re \to \infty$. Consequently, unless otherwise specified, both (5.11) and (5.12) have been used to predict the onset speeds for the hydroelastic instabilities throughout the present paper.

5.3. *Optimal wall properties*

The more compliant a wall the greater is the stabilizing effect on the TSI. See, for example, figure 11 of Carpenter & Garrad (1985). Also the greater the inertial mass of the wall the greater is the stabilizing effect on the TSI. This was demonstrated by Carpenter (1985*b*) and Willis (1986). What limits the performance of a compliant wall in the linear regime of transition is the occurrence of the hydroelastic, or flow-induced surface instabilities. Essentially, as shown by (5.11) and (5.12), increased compliance through smaller values of E, B or K_E leads to lower values of the critical speeds for divergence and TWF, while a rise in the inertial mass (i.e. $b\rho_m$) leads to a lower critical speed for the TWF. Note that, despite the appearance of the factor $(b\rho_m)^{\frac{1}{2}}$ in (5.11*b*), the critical speed of divergence does not, in fact, depend on $b\rho_m$ because of cancellation with the same factor contained in c_0 (see (2.5)). It is argued here that the optimal wall properties for any type of compliant wall must correspond to marginal stability at infinite Reynolds number with respect to the two main hydroelastic instabilities. Plainly, if the wall were any more compliant or heavier than this, hydroelastic instability would set in when a certain Reynolds number was reached and, thereby, possibly make transition delay impossible to achieve. On the other hand if the wall were any less compliant or lighter, performance in terms of transition delay would be sacrificed. It could be argued that requiring marginal stability at infinite Reynolds number is unnecessarily conservative. This may be so in some cases. But the instability mechanisms for the hydroelastic instabilities are essentially inviscid so the choice of infinite Reynolds number is not unreasonable. The question of reducing the value required for the Reynolds number corresponding to marginal hydroelastic stability is briefly discussed in §6.2. The above procedure for deriving optimal wall properties is not mathematically rigorous, but it is argued here that it makes good sense on physical grounds. Joslin & Morris (1989) have developed numerical procedures for determining the optimal wall properties for anisotropic compliant walls. Their results are close in value to those obtained by following the procedure outlined above.

Restricting the wall properties to those that are marginally stable with respect to the hydroelastic modes at infinite Reynolds number reduces the number of wall parameters very considerably. It is important to understand, however, that one or more parameters remain to be varied to achieve the best performance, according to some suitable criterion, with respect to the TSI. The restricted set of wall properties corresponding to marginal hydroelastic stability will be derived below for a non-dissipative compliant wall.

Any reduction in the number of wall parameters is certainly very helpful. There is, however, a more important advantage to be gained from using optimal wall properties when investigating the effects of anisotropic wall compliance. When an anisotropic compliant wall is compared with an isotropic one the results can be misleading if the degree of hydroelastic stability or instability is different in the two cases. The use of optimal wall properties ensures that the comparative study of the effects of anisotropic wall compliance on the growth of the TSI in the linear regime of transition is carried out on a proper basis.

To derive the optimal wall properties we first require that the critical speed for the onset of divergence be equal to the free-stream speed, thus ensuring marginal stability for divergence. From (5.11*b*) setting $U_d = U_\infty$ leads, with use of (2.5), to the following relationship:

$$B\alpha_d^3 + Eb\alpha_d \tan^2\theta + \frac{K_E}{\alpha_d \cos^2\theta} = \rho U_\infty^2. \tag{5.13}$$

Also (5.11*a*) is rearranged to obtain a second relationship of the form

$$3B\alpha_d^4 + Eb\alpha_d^2 \tan^2\theta - K_E/\cos^2\theta = 0. \tag{5.14}$$

Eliminating K_E between (5.13) and (5.14) leads to

$$B = \frac{\rho U_\infty^2}{4\alpha_d^3} - \frac{Eb\tan^2\theta}{2\alpha_d^2}. \tag{5.15}$$

Similarly when B is eliminated the result is

$$K_E = \tfrac{3}{4}\rho U_\infty^2 \alpha_d - \tfrac{1}{2}Eb\alpha_d^2 \tan^2\theta. \tag{5.16}$$

At this stage non-dimensional wall parameters are introduced. In order for the parameters to be invariant with x (or δ^*) the quantity ν/U_∞ is used as the reference length to obtain the following:

$$C_M = \frac{b\rho_m U_\infty}{\rho\nu}, \quad C_B = \frac{BU_\infty}{\rho\nu^3}, \quad C_{K_E} = \frac{K_E \nu}{\rho U_\infty^3}, \quad \bar{\alpha}_d = \frac{\alpha_d \nu}{U_\infty}. \tag{5.17}$$

Using the definition (2.3) of flexural rigidity we can write

$$Eb = \frac{12(1-\nu_P^2)B}{b^2}. \tag{5.18}$$

Substitution of (5.18) and use of the definitions (5.17) allow (5.15) and (5.16) to be rearranged in the non-dimensional forms

$$C_B = \frac{1}{4}\Big/\left(\bar{\alpha}_d^3 + 6(1-\nu_P^2)\frac{\rho_m^2}{\rho^2}\frac{\bar{\alpha}_d}{C_M^2}\tan^2\theta\right), \tag{5.19}$$

$$C_{K_E} = \left(\tfrac{3}{4}\bar{\alpha}_d - 6(1-\nu_P^2)\frac{\rho_m^2}{\rho^2}\frac{C_B\bar{\alpha}_d^2}{C_M^2}\tan^2\theta\right)\cos^2\theta. \tag{5.20}$$

Now it is required that the surface also be marginally stable with respect to TWF so that $U_{cB} = U_\infty$ in (5.12*b*). With use of (5.17) and substitution of (5.18), equation (5.12*b*) can be written in the non-dimensional form

$$1 = \frac{2(C_{K_E}C_B)^{\frac{1}{2}}}{C_M}\cos\theta + 12(1-\nu_P^2)\frac{\rho_m^2}{\rho^2}\frac{C_B}{C_M^3}\tan^2\theta\cos^2\theta. \tag{5.21}$$

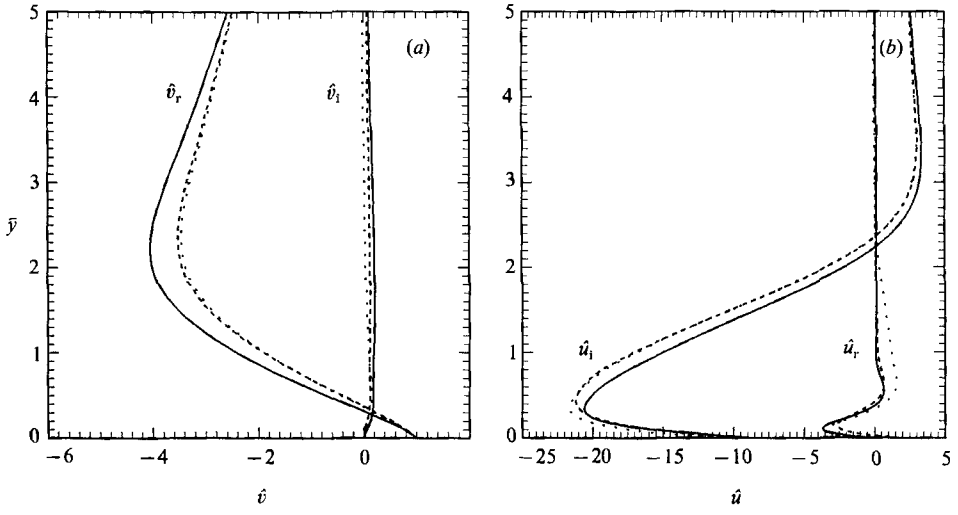

FIGURE 8. Amplitudes of disturbance for TSI corresponding to greatest growth rate at $Re = 2240$. In each case the material and fluid densities are 1000 kg/m^3, the Poisson ratio equals 0.5 and the wall parameter $\bar{\alpha}_d = 58.93 \times 10^{-6}$ (see (5.17)). ——, $\theta = 0$ ($\bar{\alpha}^* = 0.1896 - 0.00482\mathrm{i}$, $\bar{\omega}^* = 0.0651$); – – –, $\theta = 60°$ ($\bar{\alpha}^* = 0.1521 - 0.00317\mathrm{i}$, $\bar{\omega}^* = 0.0528$); ·····, $\theta = -60°$ ($\bar{\alpha}^* = 0.1476 - 0.00559\mathrm{i}$, $\bar{\omega}^* = 0.05$). The wall properties are as in table 2 for $U_\infty = 20$ m/s. (The data were supplied by R. D. Joslin of Pennsylvania State University.)

The set of three equations (5.19)–(5.21) define the optimal wall properties for a non-dissipative compliant wall. For a fixed value of θ (tacitly assuming that ρ_m/ρ and ν_p are also fixed) the three equations allow the wall parameters C_B, C_{K_E} and C_M to be obtained in terms of a single wall parameter $\bar{\alpha}_d$. The procedure adopted is quite straightforward. Equation (5.21) is solved by trial and error for C_M with (5.19) and (5.20) being used to evaluate C_B and C_{K_E} for the trial value of C_M. In this way a two-parameter family of anisotropic walls is derived which are marginally stable at infinite Reynolds number with respect to divergence and TWF. The two parameters are $\bar{\alpha}_d$, the non-dimensional critical wavenumber for divergence, and θ, the fibre angle.

Are the actual dimensional values of the optimal wall properties practically realizable? The answer to this question is postponed to §6.2 where the values of $\bar{\alpha}_d$, corresponding to the greatest reduction in TSI growth rate according to certain criteria, are determined for various values of θ.

5.4. *Mechanisms for stabilization and destabilization*

The theory outlined in §5.1 is useful for providing estimates of the eigenvalues for TWF. Its real value, however, lies in the insights it gives into the underlying physical mechanisms for stabilization and destabilization. When used in this way it applies equally well to the TSI, albeit only qualitatively. We know from the Landahl (1962)–Benjamin (1963) energy-classification scheme (see also Carpenter & Garrad 1986) that irreversible energy transfer to/from the wall will exercise a stabilizing/destabilizing influence on the Class A TSI and a destabilizing/stabilizing influence on the Class B TWF. By comparing the forms of the eigenfunctions ($\hat{v}$) shown in figures 8 and 9 it can be seen that the TSI is fundamentally a flow instability with its maximum amplitude located well above the critical point, $\bar{y}_c$, where $\bar{U} = \bar{c}_r$, whereas TWF is fundamentally an instability in the wall with its

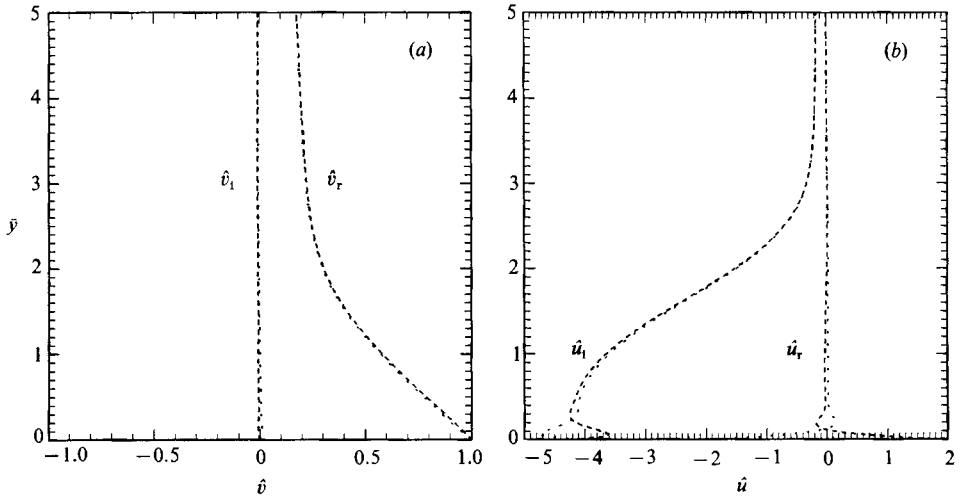

FIGURE 9. Amplitudes of disturbance velocities for TWF instability at $Re = 2240$. In each case the material and fluid densities are 1000 kg/m^3, the Poisson ratio equals 0.5, the wall parameter $\bar{\alpha}_a = 58.93 \times 10^{-6}$ (see (5.17)) and $\bar{\omega}^* = 0.14$. ---, $\theta = 60°$ ($\bar{\alpha}^* = 0.105 + 0.00141\mathrm{i}$); ·····, $\theta = -60°$ ($\bar{\alpha}^* = 0.105 + 0.00139\mathrm{i}$). The wall properties are as in table 2 for $U_\infty = 20$ m/s. (The data were supplied by R. D. Joslin of Pennsylvania State University.)

maximum amplitude at the wall itself. This distinction also explains why the transfer of energy to the wall will decrease the growth of TSI but increase that of the TWF.

Many mechanisms for irreversible energy transfer are possible for compliant walls, namely:

Energy transfer within the flow field:

energy production by Reynolds shear stress;
viscous dissipation;
energy transfer from the disturbance to the mean flow due to the interaction between the displaced mean flow and fluctuating viscous shear stress.

Energy transfer to/from the wall:

irreversible work done by the wall pressure fluctuations;
irreversible work done by the wall shear-stress fluctuations;
damping in the wall.

The contributions of the various energy-transfer mechanisms can be seen more explicitly in the integral energy equations for the flow and wall. This approach is somewhat different from that of Landahl and Benjamin and was originally inspired by the use of the energy integral equation by Stuart (1958). We were also greatly influenced by the recent work of Domaradski & Metcalfe (1987) who studied the energy balance for disturbances developing over spring-backed membrane surfaces.

For the case of two-dimensional temporally growing disturbances these equations can be written in the following forms:

$$2\omega_i \rho \int_0^\infty \overline{\tfrac{1}{2} u_i' u_i'}\, \mathrm{d}y = \rho \int_0^\infty -\overline{u'v'}\, \mathrm{D}\bar{U}\, \mathrm{d}y - \int_0^\infty \overline{\frac{\partial u_i'}{\partial x_j}\frac{\partial \sigma_{ij}'}{\partial x_j}}\, \mathrm{d}y + \overline{\dot{\eta} p_w'} - \overline{\dot{\eta}\sigma_{22w}'} - \overline{\dot{\xi}\sigma_{12w}'} + \mathrm{D}\bar{U}_w\, \overline{\eta\sigma_{12w}'}, \quad (5.22)$$

$$2\omega_i (E_K + E_S) = -\overline{\dot{\eta} p_w'} + \overline{\dot{\eta}\sigma_{22w}'} + \overline{\dot{\xi}\sigma_{12w}'} - D_W, \quad (5.23)$$

where an overbar denotes an average over a cycle, u_1 and u_2 are used for u and v, σ_{ij} denotes the various components of the viscous stress tensor, E_K and E_S denote the disturbance mean kinetic and strain energies in the wall and D_W denotes the rate of irreversible energy loss due to damping in the wall. Repeated suffices are to be interpreted as implying summation from 1 to 2. The forms of (5.22) and (5.23) are only valid if the amplitudes of the instantaneous disturbance kinetic energy in the flow and the total disturbance energy in the wall are held fixed with respect to time. Accordingly, in order to make meaningful comparisons of the sizes of the various terms in (15.22) and (15.23) the normalization condition adopted requires the disturbance kinetic-energy integral in the flow to be set equal to unity.

The energy equations and analysis developed below, like the asymptotic theory outlined in §5.1, apply equally well to general anisotropic compliant walls, including those studied by Yeo (1986, 1990). For the surface-based model described in §2, E_K and E_S can be readily derived from the equation of motion and are not integral quantities. For the more general volume-based models, including Yeo's, E_K and E_S would have to be obtained by carrying out integration across the various layers of the compliant wall.

The energy equations have been derived for the case of temporally, rather than spatially, growing disturbances. It is perfectly possible to derive an equivalent equation for spatially growing disturbances in the boundary layer (see, for example, Morris 1976). But difficulties arise when comparisons are made between the energy equations in the flow and in the wall for the spatially growing case. What, for example, is the equivalent quantity for the wall to kinetic-energy flux in the flow?

Some of the terms in (5.22) and (5.23) may require further explanation. The term on the left-hand side of (5.22) represents the rate of change of the integral of the kinetic energy of the disturbance in the boundary layer. Since temporally growing disturbances are being assumed for the energy analysis the wavenumber α in (3.1) becomes purely real and the frequency, $\omega\,(=\omega_r+i\omega_i)$, becomes complex, so that ω_i is now the temporal growth rate. This allows the time derivative of kinetic energy to be replaced by the factor $2\omega_i$. The first two terms on the right-hand side of (5.22) are respectively the rate of production of disturbance energy by the Reynolds shear stress and the viscous dissipation rate. These terms would be present for the rigid wall. They are followed by three terms representing the rate of irreversible work done to the wall by fluctuations in pressure and viscous direct and shear stresses.

The final term represents irreversible energy transfer from the disturbance to the mean flow arising from the interaction of the displaced mean flow and shear stress. To some extent this term is a consequence of the definition adopted for the mean flow. The problem has been formulated so that the Blasius profile represents the mean flow. Consequently, on the wall itself the mean flow takes the instantaneous value of $D\bar{U}_w\hat{\eta}^*$ and, accordingly, is not slowly varying there but, rather, fluctuates on the same timescale as the disturbance. Evidently, there is a problem in distinguishing the mean flow from the disturbance for flow over compliant boundaries. It has not yet been possible to establish for certain whether or not this term is always opposite in sign to the production term. The result given below, based on the asymptotic theory, suggests that for certain wall properties it could change sign and give rise to additional energy production.

Figure 10 compares the relative size of the various contributions to the energy equation (5.22) for the TSI over an isotropic compliant wall and anisotropic compliant walls with $\theta = \pm 60°$. In each case the various contributions have been normalized by setting the disturbance kinetic-energy integral to unity and (5.22) and

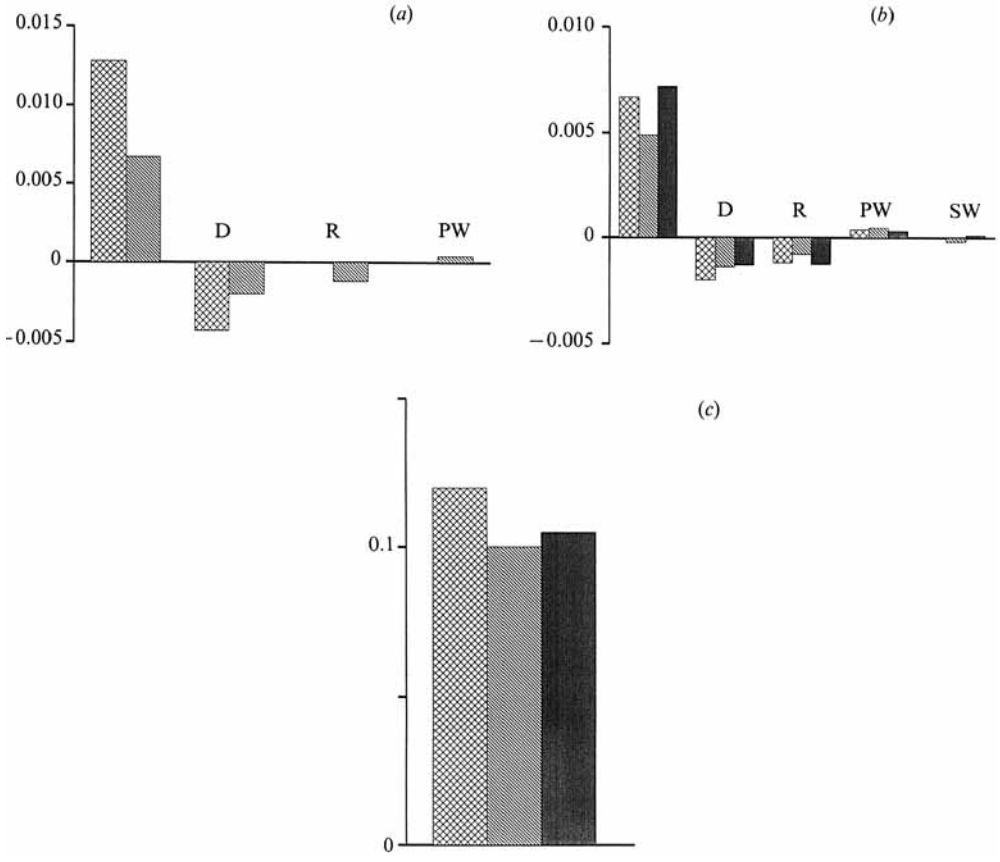

FIGURE 10. Comparisons of the sizes of various terms in the integral energy equation for temporally growing Tollmien–Schlichting waves at $Re = 2240$. The notation is as follows: P, production by the Reynolds stress; D, viscous dissipation; R, removal of energy due to interaction of wall shear stress with displaced mean flow; PW, work done by pressure at the wall; SW, work done by shear stress at the wall. (*a*) A comparison between the rigid and isotropic compliant walls. The left-hand columns correspond to the rigid wall ($\bar{\alpha}^* = 0.215$, $\bar{\omega}^* = 0.065 + 0.004\,26\mathrm{i}$) and the ones on the right to the compliant wall ($\bar{\alpha}^* = 0.190$, $\bar{\omega}^* = 0.0651 + 0.001\,54\mathrm{i}$). (*b*) A comparison between an isotropic and two anisotropic compliant walls. The left-hand columns correspond to the isotropic case of (*a*), the middle ones to $\theta = 60°$ ($\bar{\alpha}^* = 0.152$, $\bar{\omega}^* = 0.0528 + 0.001\,24\mathrm{i}$), and the right-hand ones to $\theta = -60°$ ($\bar{\alpha}^* = 0.148$, $\bar{\omega}^* = 0.0500 + 0.002\,12\mathrm{i}$). (*c*) A comparison between the total disturbance energy in the wall as a proportion of the total disturbance kinetic energy in the flow. The columns correspond to the same cases as (*b*). In all cases the data have been normalized by setting the disturbance kinetic-energy integral equal to unity, the wavenumber was chosen to be close to the value corresponding to maximum spatial growth rate and the wall properties are as figure 8. (The data were supplied by R. D. Joslin of Pennsylvania State University.)

(5.23) are both satisfied to at least three significant figures. In all three cases the wall properties are optimal in the sense of §5.3 (the values of the properties will be given in §6.2, see table 2) and the wavenumbers chosen to be close to the values corresponding to maximum instability growth rate at the given Reynolds number of 2240. The energy transfer due to work done by the direct viscous stress does not appear in figure 10. It is negligible compared to the other terms. This is to be expected since it has been found in the past that omitting this term from (2.4), and hence from (3.12), has a negligible effect on the eigenvalue. Note from figure 10 that the contribution of the energy-removal term, due to the interaction of the displaced

Energy-transfer mechanism	Change in energy-transfer rate: Isotropic *vs.* rigid wall	Anisotropic *vs.* isotropic wall: $\theta < 0$	Anisotropic *vs.* isotropic wall: $\theta > 0$	Non-zero f *vs.* $f = 0$
P in viscous wall layer	Rises	Rises	Falls	Falls
P across rest of the flow	Falls	Rises	Falls	Unknown
D	Falls	Falls	Falls	Unknown
R	Rises	Rises	Falls	Falls
PW	Rises	Falls	Rises	Rises
SW for TSI	Zero	Rises	Falls	Falls
SW for TWF	Zero	Falls	Falls	Rises if $\theta > 0$ Falls if $\theta < 0$

TABLE 1. A summary of the effects of isotropic and anisotropic wall compliance on the various energy-transfer mechanisms. The abbreviations P etc. for the energy-transfer mechanisms in the first column are defined in figure 10. Using the second column as an example, the entries in those columns, describing the change in energy-transfer rate, should be interpreted as meaning that the energy-transfer rate rises/falls for an isotropic compliant wall compared with the rate corresponding to the rigid wall and so on. The entry *zero* means that the energy-transfer rate is zero for that case, and the entry *unknown* implies that the present study has not provided the required information. The column on the extreme right provides information about the effects of wall deformation parallel to the fibre direction.

mean flow and the shear stress, is surprisingly large. This is very much in line with the results of Domaradski & Metcalfe (1987). Note also that for the TSI about 10% of the total energy resides in the wall.

Table 1 gives a summary of how the various energy-transfer mechanisms are affected by isotropic and anisotropic wall compliance. The effects of non-zero f, that is the effects of wall movement parallel to the fibre direction, are also included in the table. The results are based on the numerical results presented in figure 10 and on the asymptotic analysis given below for the various energy-transfer mechanisms. The TWF is apparently unaffected by energy transfer within the flow field, but is destabilized by energy transfer to the wall. The TSI, in contrast, is destabilized by energy transfer to the disturbances within the flow field but stabilized by energy transfer to the wall. Subject to these rules the balance achieved between the various competing energy-transfer mechanisms determines the overall effect of isotropic or anisotropic wall compliance on boundary-layer instability.

Energy production by the Reynolds shear stress

This is the primary mechanism responsible for destabilization of the TSI in boundary layer over rigid walls. In the absence of viscosity the normal and streamwise disturbance-velocity components are in anti-phase, thereby rendering the Reynolds stress zero. As originally postulated by Prandtl (1921), the effects of viscosity, especially in the critical layer, bring about the essential phase shift between the disturbance-velocity components, thereby creating non-zero Reynolds stress. This effect is still present for compliant walls. The generation of reduced, or even negative, Reynolds stress in the viscous wall layer might appear to be a plausible explanation for the stabilizing influence exercised by wall compliance on the TSI. It turns out, instead, that isotropic wall compliance actually increases the magnitude of the Reynolds stress near the wall. This is demonstrated below; see also

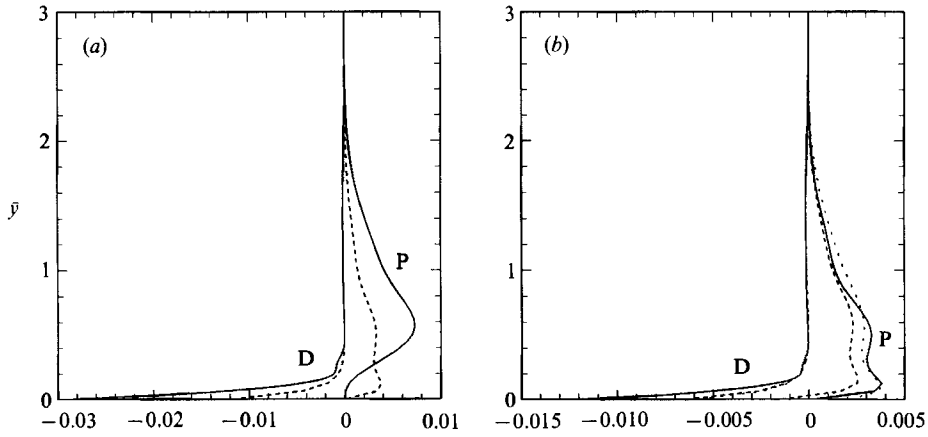

FIGURE 11. Distributions across the boundary layer of the production rate (P) of disturbance energy due to the Reynolds stress and viscous dissipation rate (D). Both quantities are normalized by setting the disturbance kinetic-energy integral in the flow equal to unity. (*a*) A comparison between the rigid and isotropic compliant walls: ——, rigid wall; – – –, isotropic compliant wall. (*b*) A comparison between an isotropic and two anisotropic compliant walls: ——, $\theta = 0$; – – –, $\theta = 60°$; ·····, $\theta = -60°$. Conditions and wall properties are as figure 8. (The data were supplied by R. D. Joslin of Pennsylvania State University.)

Domaradski & Metcalfe (1987) and Willis (1986). Even for the anisotropic compliant wall with a positive fibre angle there is only a minute region near the wall with negative energy production by the Reynolds stresses. This can be clearly seen from the distributions of normalized $-\overline{u'v'}\mathrm{D}\bar{U}$ presented in figure 11, where results for the rigid and isotropic compliant walls are compared with those for anisotropic compliant walls with positive and negative fibre angles. These results are in agreement qualitatively with those of Yeo (1986, 1990).

It would appear at first sight, then, as concluded by Yeo, that the reduction of energy production by the Reynolds shear stress near the wall at best plays a relatively minor role even for anisotropic wall compliance. It will be noted, however, in figure 11 that, with the exception of the viscous wall layer, the energy production by Reynolds shear stress across most of the boundary layer is considerably lower for the compliant walls than the rigid surface. This is reflected in the values of integrated energy production presented in figure 10. The asymptotic theory can shed little or no light on the energy production by Reynolds shear stress in the critical layer, which is the primary destabilizing mechanism for the TSI. But the theory can be used to elucidate the effects of wall compliance, including the observations made above, on the production of energy by Reynolds shear stress in the viscous wall layer. This is done below. It is important to remember, however, that the contributions to the Reynolds shear stress, which are identified below, are supplementary to the primary source of energy production in the critical layer.

The Reynolds shear stress averaged over a cycle is given by

$$-\rho\overline{u'v'} = -\rho U_\infty^2(\hat{u}\hat{v}^\dagger + \hat{u}^\dagger\hat{v}) = \frac{\mathrm{i}\rho U_\infty^2}{\bar{\alpha}^*}(\hat{v}^\dagger\mathrm{D}\hat{v} - \hat{v}\mathrm{D}\hat{v}^\dagger),$$

where $(\,)^\dagger$ denotes the complex conjugate. Ignoring $\bar{\alpha}_1^*$, (5.3) can be used with (5.9)

to show that to a good approximation the non-dimensional Reynolds stress within the viscous wall layer is given by

$$-\rho\frac{\overline{u'v'}}{U_\infty^2} \approx \tfrac{1}{2}\rho\bar{\alpha}^*|\hat{\eta}^*|^2\exp(-\tilde{y}'\sqrt{2})\left[\left\{\frac{(1-\bar{c}_r)^2}{\bar{c}_r^2}-\frac{f}{\cos^2\theta}\right\}\sin\left(\frac{\tilde{y}}{\sqrt{2}}\right)-\tan\theta\cos\left(\frac{\tilde{y}}{\sqrt{2}}\right)\right]. \tag{5.24}$$

At a fundamental level the explanation for the effect of wall compliance on the Reynolds shear stress would appear to lie with the local and long-range effects of the compliant-wall boundary conditions. In the form given in (5.3) the disturbance velocity is decomposed into a part involving an essentially inviscid fundamental solution and a part involving a viscous wall-layer solution. From this form of the disturbance velocity it can be seen that through the viscous correction C_{11} to the constant of integration C_1 in (5.3) the viscous effects at the wall influence the disturbance velocity throughout the bulk of the boundary layer. This suggests a mechanism whereby wall compliance may exercise a long-range influence possibly leading to reduced Reynolds stress, and therefore reduced energy production, across the bulk of the boundary layer, as found in figure 11. Unfortunately, since viscous effects are ignored outside the wall layer the present theory cannot be used to estimate the Reynolds stress outside of that region. It would appear from figure 11, though, that the beneficial long-range influence of wall compliance on energy production by the Reynolds stress is enhanced by anisotropic wall compliance when $\theta > 0$ but impaired when $\theta < 0$.

Irreversible energy transfer between the disturbance and the mean flow

This is due to the interaction of the displaced mean flow and the fluctuating shear stress. Substituting from (5.8) for $\hat{\tau}_w$ and (5.9) for $\hat{\xi}^*/\hat{\eta}^*$ and disregarding $\bar{\omega}_i^*$, it can be shown that for $\hat{v}_w = 1$ ($\hat{\eta}^* = \mathrm{i}/\bar{\omega}^*$) this term takes the form

$$\begin{aligned}\frac{\mathrm{D}\bar{U}_w\overline{\eta\tau'_w}}{\rho U_\infty^3} &= \mathrm{D}\bar{U}_w(\hat{\tau}_w\hat{\eta}^{*\dagger}+\hat{\tau}_w^{\dagger}\hat{\eta}^*)\\ &\approx \sqrt{2\epsilon}\mathrm{D}\bar{U}_w(\bar{\alpha}^*\bar{c}_r)^{\frac{3}{2}}\left[-\frac{(1-c_r)^2}{\bar{c}_r^2}+\tan\theta+\frac{f}{\cos^2\theta}\right].\end{aligned} \tag{5.25}$$

Irreversible work done to the wall by the fluctuating pressure

This is the primary mechanism whereby TWF is destabilized over isotropic compliant walls. Again, a phase shift in the disturbance velocity plays an essential role. In the absence of a shear layer the wall pressure would be given by the first term on the right-hand side of (5.6). Thus it can be seen that the pressure would be in antiphase with the normal velocity at the wall. Irreversible work by the fluctuating wall pressure would be zero under these circumstances. The essential phase shift occurs across the critical layer and its sign and value is determined by the term involving $\Phi_{1\infty i}$ in (5.6). If $\Phi_{1\infty i} > 0$ then the energy transfer will be to the wall. As can be seen from figure 6, $\Phi_{1\infty i}$ is positive between $\bar{c}_r = 0$ and 1 and zero for all other values. Thus the work done by the fluctuating wall pressure is destabilizing to the Class B TWF, when its phase speed falls below U_∞, and stabilizing to TSI. This mechanism was originally identified by Miles (1957, 1959*a*, *b*, 1962) in connection with water waves. His concepts were applied to compliant surfaces by Benjamin (1959, 1963).

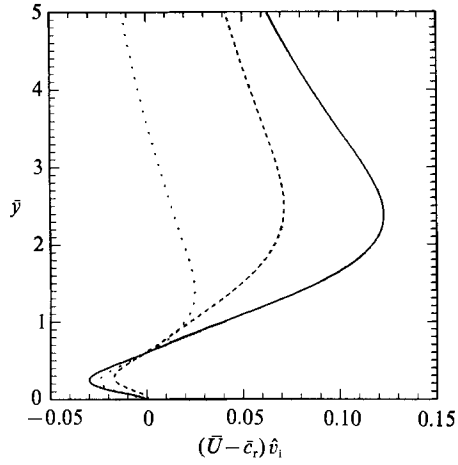

FIGURE 12. Distributions of $(\bar{U}-\bar{c}_r)\hat{v}_i$ across the boundary layer for the TSI instability. Key, conditions and wall properties are as figure 8. (The data were supplied by R. D. Joslin of Pennsylvania State University.)

The irreversible work done by wall pressure is given by

$$-\mathrm{Re}\,(p'_w\dot{\eta}) \sim \mathrm{Re}\,(\mathrm{i}\bar{\omega}^*\hat{p}_w\hat{\eta}^*) = -\mathrm{Im}\,(\bar{\omega}^*\hat{p}_w\hat{\eta}^*).$$

Thus the sign of the imaginary part of the right-hand side of (5.6) determines whether or not the energy transfer is to or from the wall. With use of (5.9) this imaginary part is given by

$$\bar{\alpha}_r^{*2}(1-\bar{c}_r^2)\,\Phi_{1\omega i}\hat{\eta}^* - \frac{\epsilon\bar{\alpha}_r^{*2}}{(2\bar{\alpha}_r^*\bar{c}_r)^{\frac{1}{2}}}(1-\bar{c}_r)^2\hat{\eta}^*\left\{\frac{(1-\bar{c}_r)^2}{\bar{c}_r^2} - \frac{f}{\cos^2\theta} - \tan\theta\right\}. \tag{5.26}$$

The first term of (5.26) corresponds to the essentially inviscid mechanism described above. The second $O(\epsilon)$ term represents the effect of an additional phase shift which occurs across the viscous wall layer. Anisotropic wall compliance modifies the viscous effect but leaves the essentially primary inviscid mechanism unaffected. Since the TWF instability sets in when $\bar{c}_r \approx 1$ the magnitude of the $O(\epsilon)$ terms in (5.26) is very small near the critical condition unless f is relatively large. Consequently one would not expect the $O(\epsilon)$ effects to be at all significant for the TWF.

The analysis given above, which was based on the asymptotic theory, is confirmed by comparing the distributions of $(\bar{U}-\bar{c}_r)\hat{v}_i$ corresponding to the TSI which are plotted in figure 12. From (5.2) we see that it is the integral of this quantity across the boundary layer that determines the sign of the imaginary part of the fluctuating wall pressure. The distributions in figure 12 indicate that energy transfer due to the work done by the fluctuating wall pressure is possible for the TSI, as shown also by the results in figure 10. A comparison with figure 10 of Carpenter & Gajjar (1990) suggests that the effect is smaller than, but of the same order as, that for TWF. The results of figure 10, however, suggest that it is a relatively unimportant effect. Figure 10 also suggests that the effect of fluctuating shear stress is relatively unimportant. In this case it is fairly easy to investigate the effect on the TSI of removing the shear stress from (3.12) (see figure 20 and §6.2), and in this way it has been established that, in fact, the effect is very significant. For this reason it is suggested that the relative size of the pressure and shear-stress work terms in (5.22) and figure 10 may be somewhat misleading when used as a guide to their relative importance for

stabilizing/destabilizing the TSI. Accordingly it is concluded here that the pressure-work mechanism is probably also important for the stabilization of TSI by wall compliance. Moreover, this mechanism is also partly responsible for the fact that anisotropic wall compliance may enhance or impair stabilization of the TSI depending on the sign of the fibre angle, θ. Note especially the proportionately larger negative contribution to

$$\int_0^\infty (\bar{U}-c_r)\,\hat{v}_i\,\mathrm{d}\bar{y}$$

from the wall region for $\theta < 0$ as compared to $\theta > 0$ in figure 12.

Irreversible work to the wall by the fluctuating shear stress

This is given by

$$\mathrm{Re}\,(\tau'\dot{\xi}) \sim -\mathrm{Re}\,(\mathrm{i}\bar{\omega}^*\hat{\tau}\hat{\xi}^*) = \mathrm{Im}\,(\bar{\omega}^*\hat{\tau}\hat{\xi}^*).$$

Now the irreversible energy transfer will be to/from the wall according as to whether the sign of $\mathrm{Im}\,(\hat{\tau}\hat{\xi}^*)$ is negative/positive. This is opposite to the correspondence between the sign of the imaginary part of the pressure and the direction of energy transfer. From (5.8) and using (5.9) the imaginary part of $\hat{\tau}\hat{\xi}^*$ is given by

$$\epsilon\hat{\eta}^*\frac{\bar{\alpha}_r^{*2}}{(2\bar{\alpha}_r^*)^{\frac{1}{2}}}\bar{c}_r^{\frac{3}{2}}\left[\frac{(1-\bar{c}_r^2)^2}{\bar{c}_r^2}\left\{\tan\theta+\frac{f}{\cos^2\theta}\right\}+\tan^2\theta-2f\tan\theta\right]. \tag{5.27}$$

Providing f is sufficiently small (5.27) is plainly positive in the case of $\theta > 0$, indicating that the irreversible energy transfer is stabilizing for TWF but destabilizing for the TSI. For $\theta < 0$ the situation is rather more complex; because, even when $f = 0$, the two remaining terms of (5.27) take opposite signs. For the TWF $\bar{c}_r$ tends to be close to 1 at the onset of instability, so that the first of these terms is generally negligible compared to the second, except for very small values of θ, when both terms are negligible. Consequently the fluctuating shear stress continues to have a stabilizing influence on the TWF even for negative θ. On the other hand for the TSI typically $\bar{c}_r \leqslant 0.4$, so that the first term of (5.27) will dominate until θ is fairly close to $-\frac{1}{2}\pi$. Thus, for TSI, fluctuating shear stress generally has a stabilizing effect when $\theta < 0$, as shown also by the results presented in figure 10.

Damping in the wall

This does not appear explicitly in the energy equation (5.22) for the flow. Nevertheless it is well known to have a destabilizing influence on the TSI, and it was this observation that originally led to the Landahl–Benjamin energy classification concept. As suggested by Domaradski & Metcalfe (1987) damping must exercise its influence indirectly by modifying the wall boundary conditions and thereby increasing the production of energy by the Reynolds stress. The fact that its destabilizing influence cannot apparently be deduced from a study of the energy equation is a good indication of the value of Landahl and Benjamin's approach. Physically, wall damping usually takes the form of viscoelastic losses, which can be modelled by introducing complex elastic moduli, or viscous losses in a fluid substrate. The modelling of these effects is discussed in Carpenter & Garrad (1985). Wall damping is always stabilizing to the TWF and almost always destabilizing to the TSI.

In summary, it may be concluded that anisotropic wall compliance will tend to stabilize the TWF instability by means of the irreversible work done by the fluctuating shear stress. This effect is almost independent of the sign of θ. For the TSI

there are many competing mechanisms of stabilization and destabilization. On balance the overall effects of anisotropic wall compliance are stabilizing for $\theta > 0$ and for small negative values of θ, but destabilizing for larger negative values of θ. These conclusions will be confirmed by the numerical results presented in §5.5 and §6.2.

Should the movement of the wall parallel to the fibres be restrained as much as possible? That is, should f be as small as possible, in order to obtain the greatest possible stabilization of the TSI? The answer to this question has important implications for the design of anisotropic and isotropic compliant walls. It is difficult to give a definite answer because, as can be seen from the analysis presented above and the results summarized in table 1, increasing f enhances some energy-transfer mechanisms but reduces others.

There is also the question of the effect of non-zero f on energy production by the Reynolds stress across the bulk of the boundary layer. This remains unanswered. In an attempt to shed some light on the overall effect of non-zero f on the stability of the TSI, some computations were carried out using the theoretical model of the compliant wall described in §2, but with (1.1) replaced by (5.10). It was found that with $f = 0.05$ there was a small reduction in the growth rate for the isotropic case, but a much larger rise in the growth rate for the anisotropic case. See the black triangles in figure 20. This rise in growth rate grew larger as θ was increased. In fact, for θ greater than about 15° the growth rates for $f = 0.05$ were off the scale of figure 20. The trends found for $f = 0.05$ persisted to much higher values of f in both the isotropic and anisotropic cases. The way that non-zero f has been introduced here is obviously rather artificial so, perhaps, too much should not be read into these results, particularly since the results in the isotropic case conflict with the contention of Gaster (1987), supported by appropriate calculations of the TSI in Daniel *et al.* (1987) that, by restricting the horizontal motion of the wall, the presence of a thin skin covering a viscoelastic substrate improved the ability of the compliant wall to reduce the growth of the TSI. The overall effect of non-zero f must, accordingly, be regarded very much as an open and important question.

5.5. *Results for the travelling-wave flutter instability*

Dispersion curves for the TWF instability are presented in figure 13 for $Re = 2240$ and $\theta = 0$, 45° and 60°. In each case optimal wall properties are used with $\bar{\alpha}_d = 58.93 \times 10^{-6}$. As noted in §6.2 this value of $\bar{\alpha}_d$ corresponds to the lowest maximum growth rate of the TSI at $Re = 2240$. The main result illustrated by figure 13 is that anisotropic wall compliance exerts a very considerable stabilizing effect on the TWF. The corresponding results for negative fibre angles are not presented: they are very little different from those in figure 13. This corroborates the conclusion made above in §5.4 regarding the indifference of the TWF to the sign of the fibre angle. Yeo (1986, 1990) came to the same conclusion.

Figure 14 shows how the suppression of various effects influences the behaviour of the TWF. When the fluctuating shear stress is omitted in (2.4) the TWF becomes slightly unstable. Moreover when all viscous effects are suppressed the resulting curve of instability growth rate versus wavenumber is very little changed from that corresponding to zero shear stress. Accordingly we may conclude that the main stabilizing mechanism for TWF, associated with anisotropic wall compliance, is the irreversible work done by the fluctuating shear stress on the wall. As shown above in §5.4 this mechanism is indifferent to the sign of the fibre angle for the TWF. Some additional stabilization is apparent at low wavenumbers. In §5.4 this was shown to

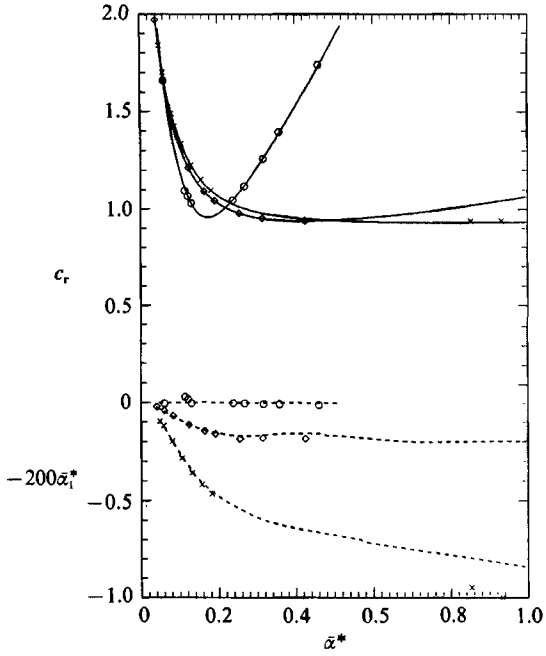

FIGURE 13. The effect of anisotropic wall compliance on the spatially developing TWF. In each case $Re = 2240$ and the wall parameter, $\bar{\alpha}_d = 58.93 \times 10^{-6}$. The wall properties for $U_\infty = 20$ m/s are given in table 2 and figure 18. The lines correspond to the results of the asymptotic theory as follows: ——, $\bar{c}_r$; – – –, $-200\bar{\alpha}_i^*$; while the discrete data points correspond to accurate numerical solutions of the Orr–Sommerfeld equation as follows: ○, $\theta = 0$; ◇, 45°; ×, 60°.

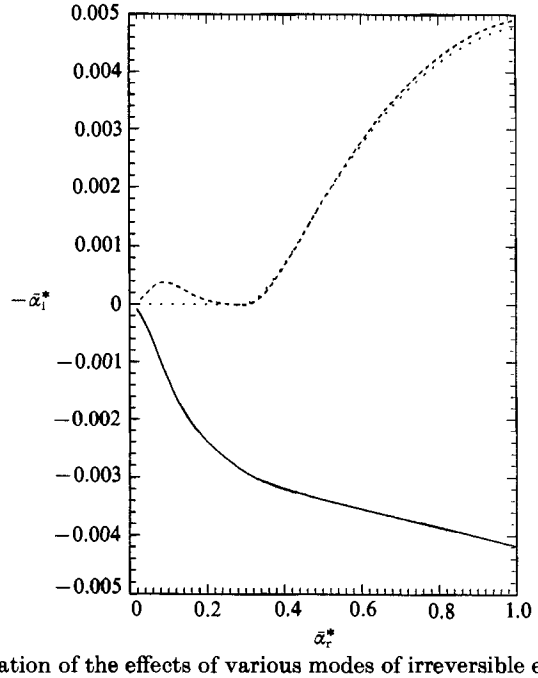

FIGURE 14. Illustration of the effects of various modes of irreversible energy transfer on the TWF. $\theta = 60°$ and $Re = 2240$. The conditions and wall properties are as for figure 13. ——, $-\bar{\alpha}_i^*$ (full viscous asymptotic theory); ·····, $-10\bar{\alpha}_i^*$ ($\hat{r}_w = 0$); – – –, $-10\bar{\alpha}_i^*$ ($\epsilon = 0$).

be due to modification by the viscous wall layer of the irreversible work done by the wall pressure.

The predictions of the asymptotic theory are compared with numerical solutions of the Orr–Sommerfeld equation in figure 13. In general the agreement is very good. However, although the phase speed is below the free-stream speed for wavenumbers above about 0.2 for the case of $\theta = 60°$, thereby ensuring the presence of a critical layer, the TWF is stable for all wavenumbers in this and the other two cases illustrated in figure 13. Accordingly, it might be felt that this is a rather inadequate test of the asymptotic theory. It is shown in Carpenter & Gajjar (1990) that the viscous effects in the critical layer make a $o(\epsilon)$ contribution to the wall pressure, so this is a higher-order effect. Nevertheless in their figure 9, which presents a comparison between the predictions of the asymptotic theory and numerical solutions of the Orr–Sommerfeld equation for an unstable isotropic compliant wall, the asymptotic theory can be seen to underestimate substantially the value of the imaginary part of the eigenvalue ($\bar{c}_i$) for temporal TWF instability. Whether this underestimate arises because of the omission of the higher-order critical layer contribution to the wall pressure, or because of some other effect associated with positive $\bar{c}_i$ (or, equivalently, in the present case, negative $\bar{\alpha}_i^*$), is not completely clear. It is known from Carpenter & Gajjar (1990) and Carpenter & Garrad (1986) that the asymptotic theory predicts the location of the neutral curve in $(\bar{\alpha}_r^*, Re)$-space with high accuracy for isotropic compliant walls. This also implies that the onset speed for the instability would be very accurately predicted.

It is for the prediction of the onset speed and neutral stability that the asymptotic theory is chiefly needed. Accordingly, it is important to try to ascertain whether or not the asymptotic theory remains accurate in this regard for anisotropic compliant walls. It turns out, however, that it is extraordinarily difficult to obtain numerical solutions of the Orr–Sommerfeld equation in the vicinity of neutral stability. The situation is exacerbated as the degree of anisotropy increases, that is as the fibre angle rises. Some idea of the problem can be had from figure 13 where the lack of data points will be noted for $\bar{\alpha}_r^*$ greater than about 0.4 for $\theta = 45°$ and $\bar{\alpha}_r^*$ between about 0.2 and 0.85 for $\theta = 60°$. The problem appears to lie with the difficulty of converging on a discrete eigenvalue in the vicinity of the continuous spectrum. (See §6.1 and figure 16 for results showing the approximate location of the continuous spectrum.) Because of these difficulties there is a paucity of data points corresponding to numerical solutions of the Orr–Sommerfeld equation in figure 15(*a*) where the neutral curves corresponding to $z_m = 1.25$ for various values of θ are presented (where z_m is the ratio of the plate thickness to the optimal value). Nevertheless good agreement is found between the neutral curves obtained from the asymptotic theory and the few data points. Good agreement was also found for eigenvalues away from the neutral curve even when convergence problems prevented solutions being obtained near the neutral curve. Thus there is no reason to assume that the asymptotic theory is not just as accurate for anisotropic compliant walls as for isotropic ones. Indeed, since the asymptotic theory is free of the convergence problems caused by the presence of the continuous spectrum, it appears to be the only feasible method of obtaining the neutral curves in the cases studied in the present paper.

It can be seen from figure 15(*a*) that, as θ rises, anisotropic wall compliance has an increasingly stabilizing effect on the TWF. This is because of the increase in the irreversible work done by the fluctuating wall shear stress as the fibre angle increases. In figure 15(*b*) the neutral curves are plotted for three values of z_m at a fixed value

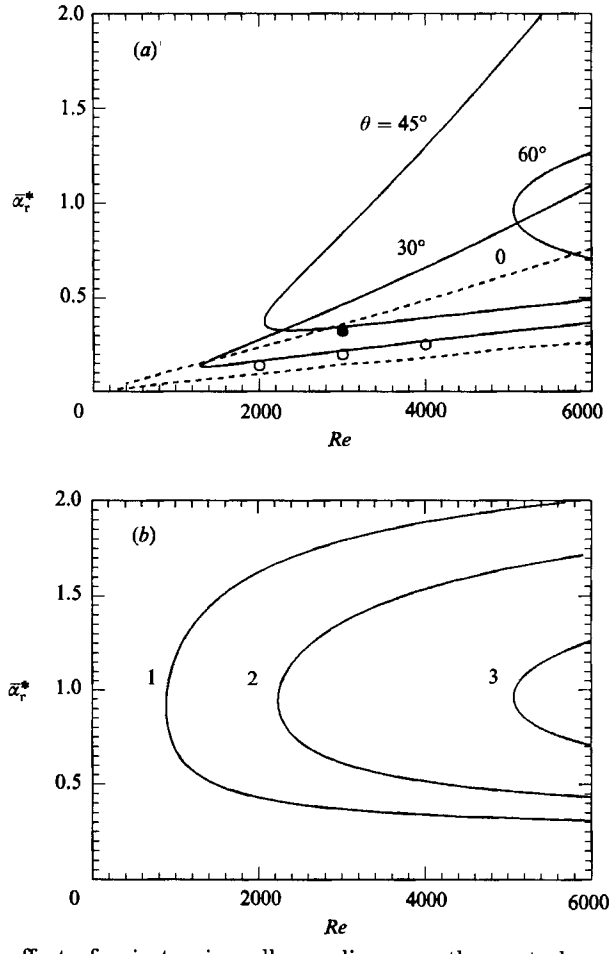

FIGURE 15. The effect of anisotropic wall compliance on the neutral curves for TWF. The wall parameter $\bar{\alpha}_d = 58.93 \times 10^{-6}$ in all cases. (*a*) Various values of fibre angle with z_m fixed at 1.25, where z_m is the ratio of the plate thickness to the optimal value given in table 2. The value of elastic modulus is chosen so as to keep the flexural rigidity equal to its value at $z_m = 1$. The data points correspond to accurate numerical solutions to the Orr–Sommerfeld equation; ○, $\theta = 30°$; ●, $\theta = 45°$. (*b*) Various values of plate mass with $\theta = 60°$. Curve 1, $z_m = 1.5$; 2, $z_m = 1.3514$; 3, $z_m = 1.25$.

of $\theta = 60°$. This shows that, as for the isotropic case, see Carpenter (1985*b*, 1987*a*), a rise in plate mass is destabilizing for TWF over anisotropic compliant walls. To calculate the wall properties for the cases shown in figures 15(*a*) and 15(*b*) the desired value of C_M was chosen and then the corresponding values of C_B and C_{K_E} were calculated from (5.19) and (5.20).

It is tempting to conclude from the results in figures 13–15 that anisotropic wall compliance could be used to suppress the TWF. On closer inspection the feasibility of this course of action would appear to depend on the way in which wall compliance is used. Thus, if the surface comprised a series of one or more relatively short compliant panels with properties tailored to the appropriate Reynolds-number range then, provided the onset of TWF could be postponed to beyond the trailing edge of a given panel, the inertial mass of the wall could exceed the optimum value given by (5.19)–(5.21). This would result in an improved performance with respect to the reduction in growth of the TSI and consequent increased transition postponement.

On the other hand, if a single relatively long compliant coating extending over a considerable Reynolds-number range were used, the onset of TWF may be merely postponed to the later stages of transition or to the fully turbulent regime. This point is illustrated by the neutral curves plotted in figure 15(*b*) which demonstrate that, for an infinitely long uniform surface, the use of anisotropic wall compliance can only postpone the Reynolds number at which TWF sets in and cannot suppress it altogether. This is only to be expected since the basic instability mechanism is fundamentally inviscid.

It may be dangerous to allow the TWF and TSI to be present simultaneously, since it is known from the work of Carpenter, Gaster & Willis (1983), Carpenter & Garrad (1985) and Willis (1986) that a powerful new instability can emerge from the coalescence of the TSI and TWF, even in the linear regime of transition. This instability is probably absolute. It has also been found in the case of anisotropic compliant walls by both Yeo (1986, 1990) and ourselves. Moreover there is the possibility of further interactions in the nonlinear transition regime. Thus, at the present state of knowledge, the only sure way to remove the danger of the TWF in the case of an extended length of compliant surface is to ensure that it is stable at all Reynolds numbers. The optimal wall properties given in §5.3 correspond to the best that can be done within this restriction. Nevertheless some results will be given for heavier compliant walls for which the critical Reynolds number for TWF is set at a finite Reynolds number.

It is worth pointing out that the remarks made above, concerning the use of anisotropic wall compliance for controlling the TWF, also appear to apply equally well to the use of damping in the wall when realistic theoretical models are used to simulate the viscoelastic material properties or the effects of a viscous fluid substrate.

6. The numerical investigation of instability and transition delay

6.1. *Results using the globally convergent scheme*

How can we be certain that all the unstable eigenvalues have been identified? In order to respond to this question the globally convergent method described in §4.3 has been used in the present study to search for all the eigenvalues. An alternative, completely different, approach to the problem is that due to Sen & Arora (1988) who, in effect, investigated all the possible motions of the compliant wall. Their method has already produced some surprising results; for example, it was shown, contrary to expectations, that the TWF could be unstable even with a phase speed in excess of U_∞. See also Carpenter & Gajjar (1990). Their method could readily be extended to the simple anisotropic compliant wall of §2. It would be difficult, however, to extend either the method of Sen & Arora or that of §4.3 to volume-based compliant-wall models like those of Yeo (1986, 1988, 1990).

Even with the globally convergent scheme it is a daunting task to establish for certain that no previously unidentified unstable eigenvalues exist for a particular compliant wall. It would be necessary to cover a large range of $\bar{\omega}$ and Re and we do not claim to have done this. We have examined a limited range of $\bar{\omega}^*$ and Re for two cases, namely the compliant walls with optimal properties having $\theta = 0$ and 60° (see table 2 for wall properties). A typical result is shown in figure 16. The eigenvalues are plotted in the form $(\bar{c}_r, \bar{c}_i)$ but, in fact, correspond to spatially growing disturbances, so $\bar{c}_r = \mathrm{Re}\,(\bar{\omega}^*/\bar{\alpha}_r^*)$ and $\bar{c}_i = -\mathrm{Im}\,(\bar{\omega}^*/\bar{\alpha}^*)$ (note that when $\bar{\alpha}^* < 0$ instability corresponds to $\bar{c}_i < 0$). Most of the eigenvalues plotted in figure 16 represent an approximation to the continuous spectrum and can be distinguished from the

θ (deg.)	Re_{MS}	$\bar{\alpha}_d \times 10^6$	b (mm)	E (MN/m^2)	K_E (GN/m^3)
0	∞	58.93	0.735	1.385	0.354
0	∞	49.11	0.882	1.385	0.295
0	∞	39.29	1.103	1.385	0.236
0	∞	29.46	1.470	1.385	0.177
60	∞	58.93	0.111	0.509	0.0590
60	∞	49.11	0.134	0.506	0.0491
60	∞	39.29	0.167	0.507	0.0393
60	∞	29.46	0.223	0.507	0.0295
60	∞	19.64	0.334	0.507	0.0197
60	∞	14.73	0.446	0.507	0.0147
75	∞	58.93	0.029	0.426	0.0158
75	∞	49.11	0.034	0.426	0.0132
75	∞	39.29	0.043	0.426	0.0105
75	∞	29.46	0.057	0.426	0.0079
75	∞	19.64	0.086	0.426	0.00526
75	∞	14.73	0.114	0.426	0.00395
75	∞	9.82	0.172	0.426	0.00263
75	2240	58.93	0.044	0.275	0.0158
75	2240	49.11	0.056	0.263	0.0132
75	2240	39.29	0.073	0.251	0.0105
75	2240	29.46	0.104	0.235	0.0079
75	2240	19.64	0.169	0.216	0.00526
75	2240	14.73	0.239	0.204	0.00395
75	2240	9.82	0.396	0.185	0.00263

TABLE 2. Optimal wall properties. Re_{MS} denotes the value of Re for which marginal stability of TWF and divergence is required

discrete eigenvalues by comparing the results obtained by using 48 and 58 Chebyshev polynomials. The eigenvalues corresponding to the continuous spectrum tend to shift as the order of the approximating polynomial is increased, whereas the discrete eigenvalues remain fixed. The three fixed eigenvalues are marked by the numerals 1, 2 and 3 in figure 16. In fact, there is also a fourth discrete eigenvalue corresponding to TWF, but for $\bar{\omega}^* = 0.055$ its value of $\bar{c}_r$ is considerably greater than unity and is therefore too large to appear in figure 16. Eigenvalue 1 corresponds to the TSI and eigenvalue 2 probably corresponds to divergence.

The appearance in figure 16 of eigenvalue 3 at first aroused both suspicion and consternation owing to its extremely large imaginary part which, according to conventional interpretation, would imply a powerful spatially growing instability. It turns out that it is a genuine eigenmode, but most probably is related to the evanescent waves described by Briggs (1964) and does not represent an instability. It is related to one of four spatially developing free-wave eigenmodes. The physical interpretation of these free wave modes and, by implication, of eigenmode 3 is revealed by the study of an initial-value problem which is loosely analogous to that formulated by Gaster (1965) to model the effects of a vibrating ribbon on a boundary layer. In this way it is established that a complex wavenumber, with a positive real part and negative imaginary part, need not represent a spatially growing instability. Eigenmode 3 and its physical interpretation will be discussed in more detail in a later paper.

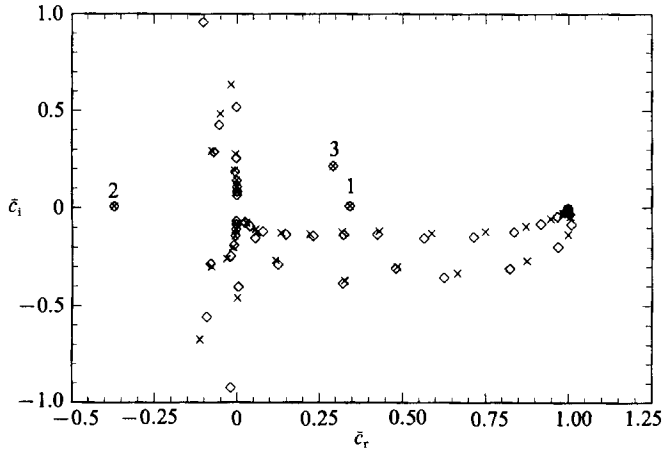

FIGURE 16. A plot of all the eigenvalues obtained by the globally convergent scheme in terms of the imaginary part of the complex wave speed ($\bar{c} = \bar{\omega}^*/\bar{\alpha}^*$) versus the real part. $\bar{\omega}^* = 0.0651$ and $Re = 2240$ for the isotropic case with the wall parameter $\bar{\alpha}_d = 58.93 \times 10^{-6}$. Properties for $U_\infty =$ 20 m/s are given in table 2. The symbols for the data points denote the following: ×, $n = 48$ Chevyshev polynomials; ◇, $n = 55$. (The data were supplied by R. D. Joslin of Pennsylvania State University.)

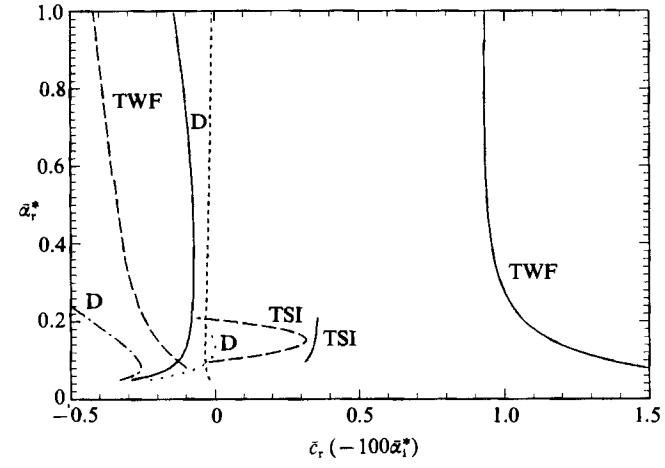

FIGURE 17. The computed divergence (D) eigenmode compared with TWF and TSI ones for $\theta =$ 60°, $Re = 2240$ and wall parameter $\bar{\alpha}_d = 58.93 \times 10^{-6}$. Properties corresponding to $U_\infty = 20$ m/s are given in table 2: ——, $\bar{c}_r$; – – –, $-100\bar{\alpha}_i^*$ ($\bar{c}_i$ for D); ·····, $\bar{c}_r$ (potential flow solution for D); —·—, $\bar{c}_r$ (asymptotic theory with $\epsilon = 0$); $\bar{c}_i$ is equivalently zero in the last two cases.

We now turn briefly to further consideration of the divergence eigenmode. In figure 17 dispersion curves are plotted for the three conventional eigenmodes in the case of an anisotropic compliant wall ($\theta = 60°$) having optimal properties (see table 2). The curve labelled D is thought to be the divergence eigenmode. It will be noted, though, that there is poor correspondence between the predictions of potential theory, or of the asymptotic theory of §5.1 with viscous effects neglected, and (temporally growing) numerical solutions of the Orr–Sommerfeld equation. The physical reasons for this are not altogether clear, but mathematically, the singular behaviour of the wall pressure, through $\Phi_{\infty 1r}$ (see figure 6), as $c_r \to -0$, is a part of the explanation. Furthermore the potential-flow theory, in effect, neglects terms of $O(\bar{\alpha}^*)$ and the asymptotic theory neglects terms of $O(\bar{\alpha}^{*2})$. These appeared to be reasonable

approximations when $\bar{c}_r \gg 0$ but only hold for $\bar{\alpha}^* < 0.05$ when $\bar{c}_r < 0$. There are also difficulties in incorporating viscous effects when $\bar{c}_r < 0$ because the viscous wall layer appears to vanish.

Temporal, rather than spatially growing, waves were used for divergence because it was difficult to obtain convergence in the spatial case. In any case it is questionable whether the spatially growing wave is a good model for divergence. In fact, the use of the Orr–Sommerfeld equation itself is also questionable. It is known (see Carpenter & Garrad 1986) that for potential flow the behaviour of the divergence-like solution over compliant surfaces of finite length differs rather fundamentally from the travelling-wave solution over an infinite surface. From the results presented by Carpenter (1990) of a computer simulation of the divergence instability for potential flow over finite isotropic compliant walls, using the methods of Lucey (1989) and Lucey, Harris & Carpenter (1989), it appears that divergence is an absolute instability which forms from a coalescence of upstream- and downstream-propagating waves. The Orr–Sommerfeld equation would not appear to be appropriate for the study of such an instability. Disregarding this point for the present, the results in figure 17 and others like them suggest that viscous effects are important for divergence and that they tend to be stabilizing. On the basis of these results, then, the prediction (5.11*b*) for critical onset speed is rather conservative.

6.2. *Presentation and discussion of main numerical results*

Many results of the numerical investigation, using the methods described in §4.1, have already been presented in §5. The effect of anisotropic wall compliance on the form of the disturbance velocity profiles (eigenfunctions) is illustrated in figures 8 and 9. The various contributions to the terms of the energy equation are presented in figure 10 for isotropic and anisotropic walls. The effects of anisotropic wall compliance on the distributions of energy production due to Reynolds stress, of viscous dissipation rate and of $(\bar{U}-\bar{c}_r^*)\hat{v}_i$ are illustrated in figures 11 and 12. The last quantity is closely related to irreversible energy transfer to the wall due to work done by the fluctuating wall pressure. Finally, data points corresponding to numerical solution of the full Orr–Sommerfeld equation are plotted in figures 13 and 15(*a*) which give the dispersion curves and neutral curves respectively for the TWF over anisotropic and isotropic compliant walls.

For many of the results presented in §5 and below, a value of $Re = 2240$ has been chosen. This value was originally selected in Carpenter (1985*b*) because it corresponds to the approximate location of maximum growth rate in a boundary layer over a rigid wall for a disturbance having the critical frequency in the e^n sense.

The concept of optimal wall properties, as outlined in §5.3, was used to select the properties for the cases previously presented and those presented below. In most cases it is required that the properties correspond to marginal stability at infinite Reynolds number with respect to the TWF and divergence. In the case of non-dissipative walls this leaves two free parameters, namely the fibre angle, θ, and the non-dimensional critical wavenumber, $\bar{\alpha}_d$, for divergence. The method used for calculating the corresponding optimal properties was briefly described at the end of §5.3. The resulting properties for a flow speed of 20 m/s, material and fluid densities of 1000 kg/m^3, Poisson ratio of 0.5 and $\bar{\alpha}_d = 58.93 \times 10^{-6}$ are presented as functions of θ in figure 18. Properties for other values of $\bar{\alpha}_d$ are given in table 2. The variation of the properties with θ is partly explained by the concept of inviscid equivalence, which leads to the relationships (5.10). Another factor is the rise in the contribution to the overall wall stiffness of the induced-tension term $Eb\,\partial^2\xi/\partial x^2 \sin\theta$

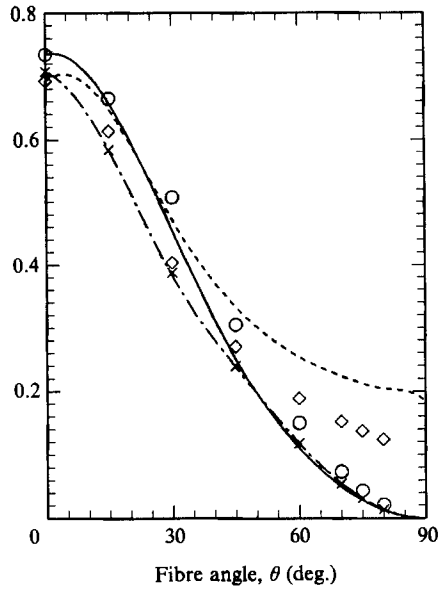

FIGURE 18. Optimal compliant wall properties as functions of fibre angle for $U_\infty = 20$ m/s. The lines correspond to marginal hydroelastic stability imposed at $Re = \infty$ as follows: ——, b (mm); – – –, $\frac{1}{2}E$ (MN/m^2); —·—, $2K_E$ (GN/m^3). The symbols correspond to marginal stability imposed at $Re = 2240$ as follows; ○, b (mm); ◇, $\frac{1}{2}E$ (MN/m^2); ×, $2K_E$ (GN/m^3).

in (2.2) as the value of θ is increased. Consequently the bending and spring stiffnesses have to be correspondingly reduced to keep the overall stiffness, and hence compliance, more or less invariant with θ.

In order to maintain dynamic similarity at other flow speeds the non-dimensional wall properties given in (5.17) must remain invariant. This invariance allows the optimal wall properties for other flow speeds to be obtained from those given in figure 18 and table 2. Thus from (5.17) it can be seen that

$$b \sim 1/U_\infty, \quad B \sim 1/U_\infty, \quad K \sim U_\infty^3, \quad E \sim U_\infty^2, \quad \alpha_d \sim 1/U_\infty. \tag{6.1}$$

The question of whether or not these properties could be realized in practice will inevitably be raised. In the case of isotropic walls in water flow it was found by Carpenter (1985*b*, 1987*a*) that the optimal properties at 20 m/s are not greatly different from the original compliant coatings of Kramer (1960). Plainly, then, the properties can be practically realized in this case and, although the optimal properties vary considerably with fibre angle, θ, no insuperable problem is anticipated in the manufacture of anisotropic compliant walls with optimal properties.

In most cases the requirement of marginal stability at infinite Reynolds number with respect to the two hydroelastic instabilities was imposed. This requirement may be considered unduly conservative. Accordingly the optimal properties were also calculated with marginal stability of the TWF imposed at a finite Reynolds number of 2240. The corresponding wall properties are to be found in table 2 and figure 18. Unless otherwise stated, though, optimal properties corresponding to marginal stability at infinite Re were used. It is somewhat more difficult to calculate the optimal properties corresponding to marginal stability at finite Re. The procedure adopted is as follows. The optimal properties corresponding to marginal stability at

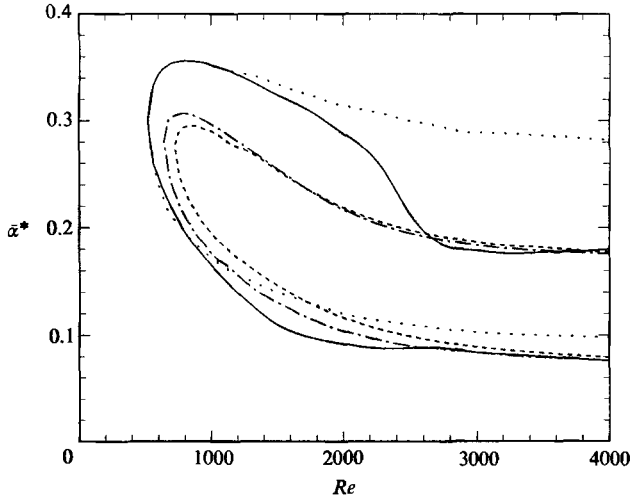

FIGURE 19. Effect of anisotropic wall compliance on neutral-stability boundaries for TSI. The wall parameter $\bar{\alpha}_d = 58.93 \times 10^{-6}$. ·····, Rigid wall; ——, $\theta = 0$; —·—, $\theta = 60°$; – – –, $\theta = 75°$. The wall properties corresponding to $U_\infty = 20$ m/s are given in table 2.

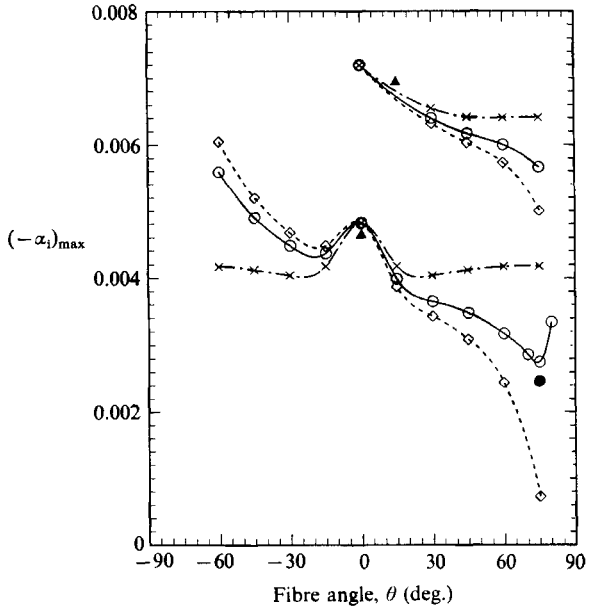

FIGURE 20. The effect of anisotropic wall compliance on the maximum growth rate of the TSI with wall parameter $\bar{\alpha}_d = 58.93 \times 10^{-6}$. The wall properties corresponding to $U_\infty = 20$ m/s are given in figure 18. The upper set of curves correspond to $Re = 5000$, the lower to $Re = 2240$. The data points correspond to the actual computed values as follows: ○, solution with all terms included; ◇, solution with $\hat{\tau}_w = 0$; ×, solution with $\xi = 0$; in the foregoing cases marginal hydroelastic stability was imposed at $Re = Re_{MS} = \infty$, ● corresponds to a case for which $Re_{MS} = 2240$. ▲ corresponds to the case for which $f = 0.05$ and $Re = 2240$.

$Re = \infty$ are used as a starting point. The plate thickness and elastic modulus are then varied by trial and error, keeping the flexural rigidity, spring stiffness and $\bar{\alpha}_d$ fixed, until a larger value of plate thickness is found for which the TWF is neutrally stable at some value of $\bar{\alpha}^*$ and stable for all other values. This is achieved by using the

asymptotic theory of §5.1 to obtain accurate approximations to the Orr–Sommerfeld equation, as in §5.5. The use of full numerical integration of the Orr–Sommerfeld equation for this purpose would have involved a prohibitively large amount of computational work. It also may well have not been possible to obtain the desired numerical solutions owing to the convergence problems (see §5.5) associated with the presence of the continuous spectrum.

Computed neutral curves are presented in figure 19 for the rigid wall and for compliant walls with $\theta = 0$, 60° and 75°. It can be seen that the region of instability in $(\bar{\alpha}^*, Re)$-space becomes progressively smaller as θ rises.

With the help of the computed results presented to illustrate §5 and summarized in table 1 it has been established that the principal way in which anisotropic wall compliance reduces the growth of the TSI is by the reduction of the energy production due to Reynolds stress. Irreversible energy transfer from the disturbance to the mean flow due to the interaction of fluctuating viscous shear stress and the displaced mean flow, also makes an important contribution. The effect of reduced Reynolds stress is enhanced for anisotropic walls with $\theta > 0$ and diminished for $\theta < 0$. The unfavourable effects associated with $\theta < 0$ are ameliorated to a considerable extent by a rise in the energy-removal rate due to shear-stress/displaced-mean-flow interaction when $\theta < 0$ and by the effects of irreversible energy transfer to the wall due to the work by the fluctuating shear stress. The latter is stabilizing for the TSI when $\theta < 0$ and destabilizing when $\theta > 0$. The balance of these various energy-transfer mechanisms is reflected in the results plotted in figure 20. There the maximum growth rate of the TSI is plotted against θ for fixed $\bar{\alpha}_d$ and Re.

It will be noted from figure 20 (solid lines) that, unless the magnitude of θ is small, the growth rate for positive fibre angles is considerably less than that for the isotropic case, while that for negative fibre angles is considerably more. At $Re = 2240$ the optimum fibre angle appears to be about 75°. This is clearly Reynolds-number dependent since no minimum was reached at $Re = 5000$, although presumably one does occur at sufficiently high values of θ. For small absolute values of θ the growth rate is reduced compared to $\theta = 0$ irrespective of the sign of θ. This can be explained by the trade-off between the various energy-transfer mechanisms as adumbrated in the previous paragraph. The effects of energy transfer due to the irreversible work done by the fluctuating shear stress is clearly depicted in figure 20. Note the broken lines corresponding to computations for which $\hat{\tau}_w$ has been set equal to zero in (2.4) and (3.12). It can be seen immediately that this mechanism is stabilizing when $\theta < 0$ and destabilizing when $\theta > 0$; the latter effect being the stronger. As expected, since this is essentially a viscous effect, the difference between the growth rates with and without τ_w is much reduced at the higher Re of 5000. This is very much in line with the predictions of the asymptotic theory presented in §5.4. The large difference between the growth rates with and without τ_w for $\theta \geqslant 60°$ and $Re = 2240$ is worth noting. Based on the relative size of the various terms of the energy equation presented in figure 10 one could be forgiven for concluding that energy transfer due to the irreversible work done by the fluctuating shear stress played a very minor role. The results presented in figure 20 make it plain that this is far from the case. Accordingly, it is suggested that energy transfer due to irreversible work done by the fluctuating wall pressure probably also makes a significant contribution to the overall stabilization/destabilization mechanisms. Evidently it is unwise to try to make quantitative predictions based on the relative size of the various terms in the energy equation.

Also shown in figure 20 (see the dash-dot lines) are the results obtained when

horizontal displacement, ξ, is set equal to zero in (2.4) and (3.12). In this case, as expected, the growth rates are invariant with the sign of θ. The growth rate falls with small values of θ and then rises gradually. This is because the flexural rigidity, spring stiffness and plate thickness all decrease with a rise in θ. A decrease in stiffness is stabilizing whereas a reduction in plate mass is destabilizing. For low values of θ the first effect dominates while at higher values the destabilizing effect of reduced plate mass dominates. The results for $\xi = 0$ in figure 20 demonstrate convincingly that the considerable reduction in TSI growth rate found for positive fibre angles is not just a result of a favourable change in wall compliance, but is very much dependent on the horizontal motion of the wall. It is also clear that the effect is predominantly viscous, since again the difference between the growth rates with and without horizontal motion are much reduced at the higher Reynolds number of 5000.

Some computations have been carried out for optimal wall properties obtained by imposing marginal TWF stability at $Re = 2240$ instead of ∞. This leaves the optimal properties almost unchanged in the isotropic case of $\theta = 0$ but makes a substantial difference as θ becomes larger. In figure 20 the data point denoted by the black circle corresponds to the ($Re = 2240$) optimal properties at $\theta = 75°$. It can be seen that a further 10% reduction in maximum growth rate is obtained.

Also included in figure 20 are two results, denoted by the black triangles, of calculations with non-zero f. Further explanation is to be found towards the end of §5.4.

Since it appears from figure 20 that the optimum fibre angles are fairly large it is interesting to speculate on the limiting case of $\theta = 90°$. No calculations were carried out for $\theta > 80°$: it became increasingly more time-consuming to perform calculations at these high values of θ. From the results obtained it appears that the optimal values of spring stiffness and plate thickness both tend to zero as $\theta \to \frac{1}{2}\pi$. This is reflected in figure 18. Moreover, it is what emerges from investigating the behaviour of (5.19)–(5.21) in the limit as $\theta \to \frac{1}{2}\pi$. However, it should be noted that it is tacitly assumed that the optimal value of $\bar{\alpha}_d$ remains fixed as the limit of $\theta = \frac{1}{2}\pi$ is approached. There is no evidence that this is not a good assumption, but its validity has not been established for certain. If the limiting values of the optimal properties are correct then there can be little practical interest in the case of $\theta = \frac{1}{2}\pi$. Furthermore, it can be seen from figure 20 that there is a very steep rise in TSI growth rate once the optimal fibre angle is exceeded. This is undoubtedly a result of the increasing dominance of irreversible energy transfer due to the work done by the fluctuating shear stress.

The results of the e^n-type calculations, described in §4.2, are considered now. Maximum-amplification envelopes for various values of $\bar{\alpha}_d$ are presented in figures 21 and 22 for $\theta = 0$ and 60° respectively. The curves are envelopes of individual curves of the ratio of the disturbance amplitude to its initial value at neutral stability versus Re for fixed values of frequency. Some of these fixed-frequency amplitude curves are plotted in figure 22. It can be seen from figure 21 that for the isotropic compliant wall the maximum-amplification envelopes assume a characteristic sigmoid shape. As the value of $\bar{\alpha}_d$ is reduced the local minimum moves to higher values of Re. The local minimum corresponds to the Reynolds number for which the wall properties are optimal with respect to instability growth. Thus the results for $\bar{\alpha}_d = 58.93 \times 10^{-6}$ correspond to optimization with respect to TSI growth rate at about $Re = 2240$. It is also plain from figure 21 that, once a value has been selected for n, it is the size of the local maximum in the maximum-amplification envelopes that limits the 'transitional' Reynolds number attained with use of isotropic wall compliance. For

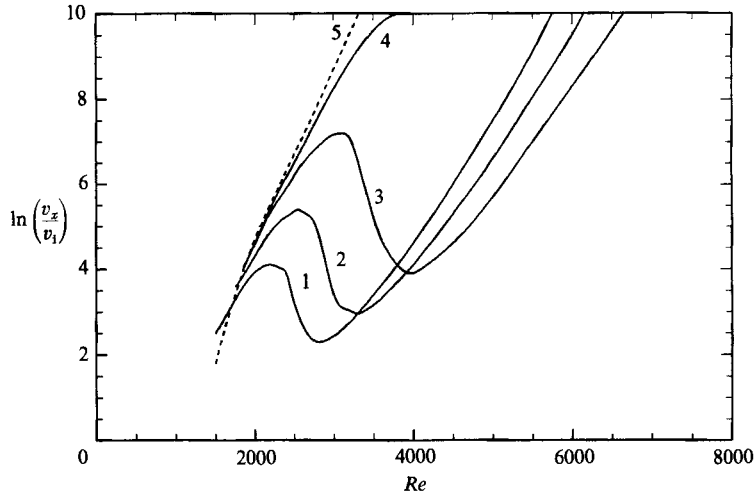

FIGURE 21. The maximum amplification envelopes as functions of Re for various optimal isotropic compliant walls. Curve 1, $\bar{\alpha}_d = 58.93 \times 10^{-6}$; 2, $\bar{\alpha}_d = 49.11 \times 10^{-6}$; 3, $\bar{\alpha}_d = 39.29 \times 10^{-6}$; 4, $\bar{\alpha}_d = 29.46 \times 10^{-6}$; 5, rigid wall. The wall properties corresponding to $U_\infty = 20$ m/s are given in table 2.

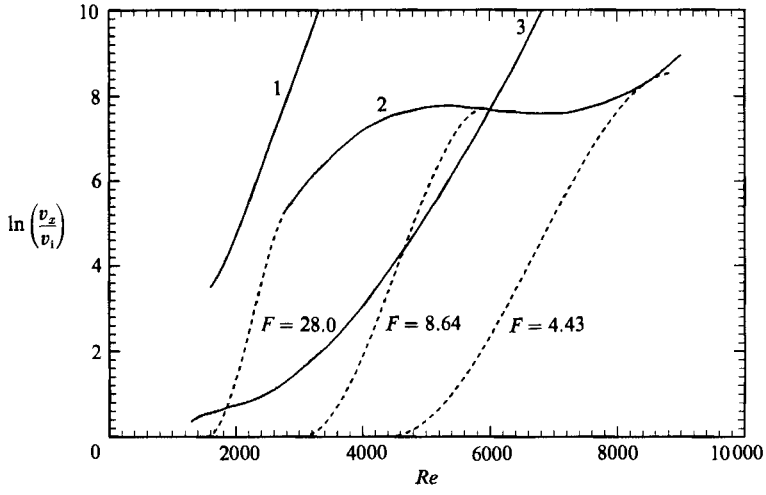

FIGURE 22. The maximum amplification envelopes as functions of Re for two optimal anisotropic compliant walls with $\theta = 60°$. ——, Curve, 1, rigid wall; 2, $\bar{\alpha}_d = 14.73 \times 10^{-6}$; 3, $\bar{\alpha}_d = 58.93 \times 10^{-6}$; —— $\ln(\hat{v}_x/\hat{v}_1)$ vs. Re for fixed frequency ($F = \bar{\omega}^* \times 10^6/Re$). The wall properties corresponding to $U_\infty = 20$ m/s are given in table 2.

carrying out predictions of transitional Reynolds number a relatively conservative value of $n = 7$ has been used. This corresponds approximately to the limit of the linear regime of transition over rigid walls in conditions of very low free-stream disturbance. The transition-delay factor, defined as the ratio of Re_x corresponding to $n = 7$ for the compliant wall to that for the rigid flat plate, is plotted in figure 23 as a function of $\bar{\alpha}_d$. The sharp fall for $\theta = 0$ (and similar ones for the anisotropic walls), which occurs at about $\bar{\alpha}_d = 40 \times 10^{-6}$, corresponds to the case when the local maximum reaches $n = 7$ in figure 21 (i.e. Curve 3). This case can be regarded as corresponding to the best performance, based on $n = 7$, for a non-dissipative isotropic compliant wall. The distance from the leading edge to the end of the linear

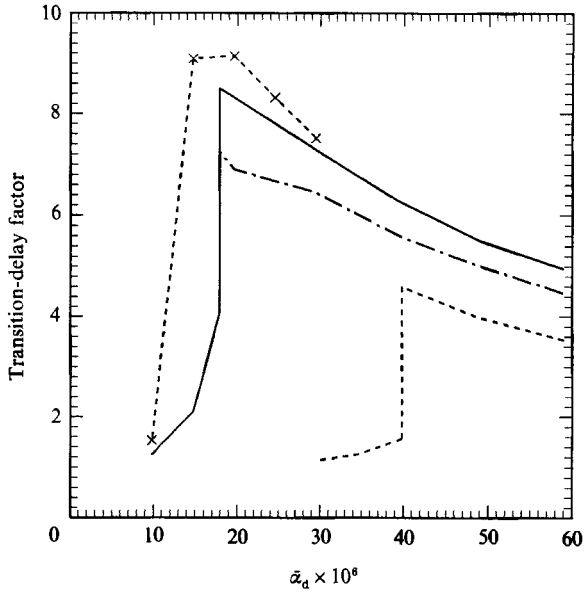

FIGURE 23. The relative increase in the length of the linear transition regime as a function of the wall parameter $\bar{\alpha}_d$ for various anisotropic and isotropic compliant walls. The transition-delay factor is defined as the ratio of the value of Re_x corresponding to $n = 7$ in a particular case to that for the rigid wall. ---, $\theta = 0$; —·—, $\theta = 60°$; ——, $\theta = 75°$; in the foregoing cases marginal hydroelastic stability was imposed at $Re = Re_{MS} = \infty$, — × —, corresponds to the case for which $Re_{MS} = 2240$ for $\theta = 75°$.

regime of transition is predicted to be 4.5 times greater than for the corresponding rigid wall in this case.

Two cases for $\theta = 60°$ are plotted in figure 22. One curve corresponds to $\bar{\alpha}_d = 58.93 \times 10^{-6}$, the other to $\bar{\alpha}_d = 14.73 \times 10^{-6}$. Note that $n = 7$ is slightly exceeded at relatively low Re in the second case. In contrast to the isotropic case illustrated in figure 21 the maximum-amplification envelopes for the anisotropic compliant wall do not exhibit the characteristic sigmoid shape so clearly. There is a very slight local maximum and minimum for Curve 2 in figure 22, but essentially it remains fairly flat for a considerable range of Reynolds numbers. Thus the optimal properties of anisotropic compliant walls are not finely tuned to the local Reynolds number as are those for the isotropic walls. This, along with reduced growth rates, leads to a considerably improved performance compared to isotropic compliant walls. The reason for the reduced sensitivity to Reynolds number remains to be fully explained. It is suggested here that it comes about because of the reduced contribution by the flexural rigidity to the overall wall stiffness. The term containing B in (3.12), see (3.10) also, involves $\bar{\alpha}^{*4}$, whereas the tension and spring-stiffness terms are less heavily dependent on wavenumber. Further evidence that walls without bending stiffness are far less sensitive to Reynolds number, is to be found in Carpenter (1985*b*). There is was found that the maximum growth rates for TSI in boundary layers over spring-backed tensioned membranes with optimal properties varied much less with $\bar{\alpha}_d$ than those for plate/spring compliant walls.

The increase in the extent of the linear regime of transition for anisotropic compliant walls with $\theta > 0$ is shown by the results plotted in figures 23 and 24. The latter shows the transition-delay factor as a function of θ keeping $\bar{\alpha}_d$ fixed at 58.93×10^{-6}, while figure 23 depicts the variation of this quantity with $\bar{\alpha}_d$ for $\theta = 60°$

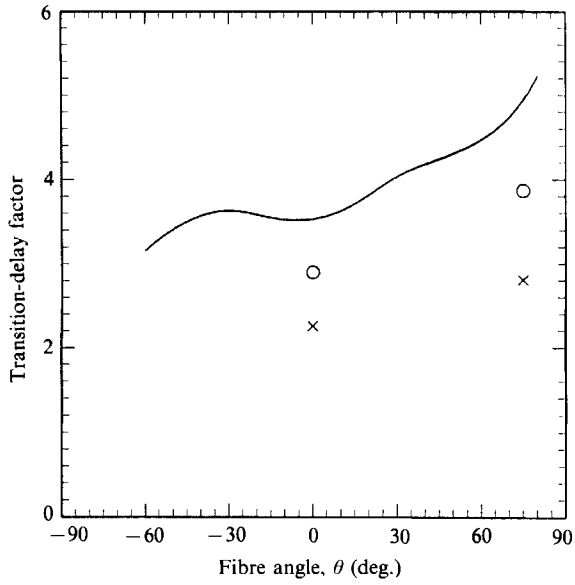

FIGURE 24. The relative increase in the length of the linear transition regime as a function of fibre angle keeping the wall parameter $\bar{\alpha}_d$ fixed at 58.93×10^{-6}. Transition-delay factor is defined as in figure 23 and the wall properties corresponding to $U_\infty = 20$ m/s are given in figure 18; the properties for negative θ are the same as for the corresponding positive angle. The data points correspond to wall damping as follows: ○, $\bar{\eta} = 0.05$; ×, $\bar{\eta} = 0.1$.

and 75°. It can be seen from figure 24 that for negative fibre angles the 'transitional' Reynolds number remains practically unchanged until $\theta = -45°$. For positive fibre angles there is a steady rise in 'transitional' Reynolds number as θ increases. When $\bar{\alpha}_d$ is reduced in value as in figure 23 the advantages of anisotropic wall compliance becomes even more pronounced. The 'transitional' Reynolds number is predicted to reach as much as 7 and 8.5 times the rigid-wall value for $\theta = 60°$ and 75° respectively. If the conditions on marginal stability for the TWF are relaxed, and the Reynolds number required is reduced from infinity to 2240, an even more impressive extension of the linear transition regime is obtained, as seen in figure 23. Thus it can justly be claimed that in theory almost a ten-fold rise in transitional Reynolds number is possible with the use of anisotropic wall compliance.

Owing to the sensitivity of the optimal wall properties to Reynolds number it is natural to speculate on the possibility of tailoring the wall properties for a particular Reynolds-number range. Probably the most practical way to achieve this is to construct a compliant surface from a series of panels in tandem (and possibly in parallel as well). One can easily envision a further improvement in performance with this arrangement, especially as it is likely to confer increased stabilization with respect to the hydroelastic instabilities, thereby allowing the use of heavier and more flexible walls. At present there is no information, either experimental or theoretical, to offer guidance on just how small a compliant panel may be without significantly impairing the stabilizing effect on the TSI. From the point of view of the eventual technological exploitation of compliant walls for transition postponement this is an important practical problem.

Three-dimensional effects should also be mentioned. It was shown by Yeo (1986), Carpenter & Morris (1989) and Joslin *et al.* (1990) that, for compliant walls with good transition-delaying properties, oblique TSI tend to have a higher growth rate than

the corresponding two-dimensional instabilities. It is easy to see why this should be so. The effective wall compliance increases with flow speed, while the effective flow speed for an obliquely propagating wave is less than U_∞. Thus oblique waves experience decreased effective wall compliance compared to two-dimensional ones. This has a relative destabilizing effect on the oblique TSI which can dominate the stabilizing effect of reduced effective Reynolds number. The relative dominance of the oblique waves is highly Reynolds-number dependent and is postponed to higher Reynolds number for smaller values of $\bar{\alpha}_d$. Anisotropic wall compliance seems to confer advantage with regard to the dominance of the oblique waves. The higher the value of θ the less the dominance of the oblique waves. This appears to be because the energy transfer due to irreversible work done by the fluctuating shear stress (which, as shown above, has a destabilizing effect on the TSI) is reduced for oblique waves. Nevertheless the results of the e^n-type calculations presented in figures 23 and 24 may need to be modified when three-dimensional effects are taken into account.

It appears from the results of the present study that, in almost every respect, anisotropic compliant walls with positive fibre angles confer advantage for transition postponement compared to their isotropic counterparts. In one respect, however, isotropic wall compliance has the advantage. It appears to be less sensitive to wall damping. This is illustrated by the data points plotted in figure 24. In order to perform these calculations E is replaced by the complex quantity $E(1-i\tilde{\eta})$ in (2.4) and B and K_E are similarly treated. In this way viscoelastic effects can be simulated. $\tilde{\eta}$ can be regarded as the viscoelastic loss factor. e^n-type calculations were carried out for $\tilde{\eta} = 0.05$ and 0.1, which are typical values for elastomers. It can be seen from figure 24 that the deleterious effects of wall damping are proportionately larger for $\theta = 75°$ than for $\theta = 0$. It should be feasible to manufacture fibre-composite anisotropic walls with low damping ($\tilde{\eta} \approx 0.01$ or less), so this should not prove a major drawback for the application of anisotropic wall compliance.

There is another consequence of the greater sensitivity of anisotropic compliant walls to damping. Carpenter (1985*b*) found that, provided the value of Re required for marginal hydroelastic stability were relaxed from infinity to a finite value (say $Re = 2240$), then damping could be used to control the TWF. This allowed heavier compliant walls to be used with a consequent improvement in performance. The wall mass (or, equivalently, the plate thickness) could be increased by a factor of up to about three times the value corresponding to $Re_{MS} = \infty$ given in table 2. Greater wall masses than this gave rise to the powerful instability which occurs when the TSI and TWF coalesce (see Carpenter *et al.* 1983; Carpenter & Garrad 1985; and Willis 1986). For anisotropic compliant walls with $\theta \geqslant 60°$ a much smaller rise in wall mass led to modal coalescence in the present study. This is probably because in the case of anisotropic compliant walls with positive fibre angles the irreversible energy transfer due to the work done by the fluctuating shear stress already exercises a damping-like effect. Thus the effective damping is considerably higher than the viscoelastic damping in this case. It should be made clear, however, that our investigation of the effects of damping has not been comprehensive.

Finally, it may be worth speculating briefly on whether or not anisotropic wall compliance has been exploited by nature. Most diagrams and photographs of cross-sections of the dolphin epidermis (e.g. see Carpenter & Garrad 1985, figure 2) make it appear as if the dermal papillae are vertical. In fact, according to Babenko & Surkina (1969) the angle made by the dermal papillae to the surface varies very considerably, but in a organized fashion, from 10° to 90° over the body of the dolphin. Now, from the present study, it appears that one of the principal factors

that limits what can be achieved in transition control by the use of anisotropic wall compliance is the irreversible energy transfer due to the work done by the fluctuating shear stress. It is certainly probable that this deleterious effect will be strongest in regions of favourable external pressure gradient, where the mean skin friction is greatest, and weakest in regions of adverse external pressure gradient, where the mean skin friction is lowest. It may be merely coincidental, of course, that the incidence of the dermal papillae tends to be in the region of 10° to 25° over the head and 55° to 80° behind the dorsal fin and just ahead of the flippers.

6.3. *Comparison with the results of Yeo*

Yeo (1986, 1990) has developed approximate volume-based models for single- and double-layer fibre-composite anisotropic compliant walls and conducted a thorough numerical study of boundary-layer stability and transition over such surfaces. Before comparing his results and conclusions with those of the present study the two main shortcomings of Yeo's approach should be noted. First, no account was taken of the divergence instability. Thus we have no way of knowing whether or not the occurrence of this instability could have prevented the realization of some of the substantial reductions in TSI growth rate found by Yeo (1986, 1988, 1990) for certain of his isotropic and anisotropic compliant walls. Secondly, he did not use optimal wall properties in the sense of §5.3. His usual practice was to vary a particular wall property, like fibre angle for example, keeping the other properties fixed. The drawback with this approach is that the stability characteristics of the TWF usually change substantially as this property is varied. Hence the TWF may be more strongly unstable for some values of the varying property than for others. This is clearly evident for some of Yeo's neutral-stability curves. Consequently the comparisons of the effect on the TSI between one case and another are not on a completely firm footing. In contrast, with the present approach the properties are varied so that the TWF (and divergence) are marginally stable at $Re = \infty$ or some other specified value. Thus with the present approach there is no danger that any gains achieved for the TSI have to be offset against destabilization of the TWF mode. These comments are not intended as criticisms of Yeo's work but, rather, the shortcomings stem from his attempt to use a more realistic theoretical model than that of the present study. It is simply not possible with our present state of knowledge to predict the divergence instability or to carry out the optimization of wall properties for a volume-based model of an anisotropic compliant wall.

The maximum-amplification envelopes (n. vs. Re_δ curves) of Yeo are quite similar to those obtained in the present study for both isotropic and anisotropic walls. His anisotropic curves were more sigmoid in shape than those in figure 22, but this is probably because his fibre angles were not as large: Yeo's fibre angle A_f is measured from the vertical whereas θ is measured from the horizontal. His predicted transitional Reynolds numbers are also comparable with those of figures 23 and 24. His conclusion that the TWF instability is independent of the sign of the fibre angle is also completely supported by the results of the present study (see §5.5).

The results of the present study do not support his conclusions with regard to the effect of the sign of the fibre angle on the TSI. He concludes that: 'Since the TSI regimes at large Reynolds numbers are largely unaffected by the sign of A_f, it is not unreasonable to deduce that significant gains in stability (and projected transition distance) .... are to a large measure the consequences of some desirable changes to the compliant qualities of the wall.' The present results show quite conclusively that increased stabilization of the TSI comes about from a variety of mechanisms,

principally reduced production of disturbance energy by the Reynolds stresses, all of which are sensitive to the sign of the fibre angle. Moreover, some of the results given in figure 20 show conclusively that the reduced growth rates are not just a consequence of desirable changes to the compliant qualities of the wall, but are inherently a consequence of the wall having horizontal, as well as vertical, motion. Although the additional stabilization found with anisotropic wall compliance is associated with viscous effects and, therefore, becomes weaker at higher Reynolds number, it is nevertheless found to persist to a sufficient degree at large Reynolds numbers, resulting in predictions of a very substantial postponement of laminar/turbulent transition.

Why are Yeo's conclusions in conflict with those of the present study? The principal reason would appear to be that his fibre angles A_f were rather large. Thus one of his main comparisons of the effects of positive and negative fibre angles was carried out for $A_f = \pm 60°$ (i.e. $\theta = \pm 30°$). At such low values of θ there is not much to choose between the positive and negative orientation, as can be seen from figure 20. This is because the effects of energy transfer due to the work done by the fluctuating shear stress and the rise in the energy transfer from the disturbance to the mean flow due to the interaction of the fluctuating shear stress and the displaced mean flow partially offset the effects of increased production and reduced pressure work in the case of negative fibre angle. Also, in the case of Yeo's walls there was a certain amount of displacement parallel to the fibre direction (see figure 7) and, as was shown in §5.4, this reduces the differences between positive and negative fibre angles. Be that as it may, Yeo's actual results are not in conflict with the conclusions of the present study. For example his neutral curves (figure 13*b* of Yeo 1990) show that the regions of instability are greater for negative than positive fibre angles. Furthermore his distributions for normalized Reynolds stress (figure 23 of Yeo 1990) show that the production of energy would be considerably greater for the negative than positive fibre angles. This is notwithstanding the miniscule contribution of the region of negative Reynolds stress noted by Yeo in the latter case. Accordingly it is suggested here that Yeo's conclusion on the effect of fibre orientation on the TSI are not correct in general, but his actual results are fully compatible with the conclusions of the present study.

7. Conclusions

A relatively simple surface-based theoretical model of an anisotropic compliant wall has been developed and a numerical investigation of its effects on boundary-layer instability and transition carried out. An asymptotic theory has also been used, together with a study of the energy equation, to elucidate the mechanisms of instability for more general compliant walls. The following are the main practical conclusions to be drawn from the present study:

Anisotropic wall compliance with positive fibre orientation confers considerable advantage with respect to reduction in instability growth rate and transition delay. An almost ten-fold increase in transitional Reynolds number is predicted for anisotropic walls having the appropriate properties.

The reduction in the growth of Tollmien–Schlichting waves by the use of wall compliance is a result of a favourable balance being established between several competing energy-transfer mechanisms, including those found for the rigid wall, namely energy production by the Reynolds stress and viscous dissipation. However, since viscous dissipation is insensitive to the sign of the fibre angle, the particularly

favourable effect of anisotropic wall compliance with positive fibre angle may primarily be attributed to a reduction in the production of energy by the Reynolds stress. Even so the other mechanisms of energy transfer remain important and the overall balance between them is such that for fairly small fibre angles anisotropic wall compliance has a favourable effect regardless of the sign of the fibre angle.

Some of the other mechanisms for stabilization/destabilization are also sensitive to the sign of the fibre angle. For example, irreversible energy transfer from the disturbance to the mean flow occurs owing to the interaction of the fluctuating shear stress and displaced mean flow. In all the cases studied this mechanism resulted in energy being removed from the disturbance, but there appears to be a possibility of additional energy production for certain combinations of wall properties. The energy loss is relatively greater for negative fibre angles, and therefore makes a greater contribution to reducing the instability growth rate in that case. Irreversible energy transfer to/from the wall due to the work done by the fluctuating wall pressure and shear stress also plays a significant role. The shear-stress work is destabilizing (stabilizing) to the Tollmien–Schlichting waves for positive (negative) fibre angles. The work done by wall pressure is stabilizing and increases for positive angles but decreases for negative angles.

The optimal properties of anisotropic compliant walls appear to be much less sensitive to Reynolds number than those corresponding to isotropic walls.

The travelling-wave flutter and divergence instabilities are insensitive to the sign of the fibre angle. Anisotropic wall compliance has a considerable stabilizing effect on the former and viscous effects become much more important than for the isotropic case.

Wall displacement parallel to the fibre direction has a mixed effect on the various energy-exchange mechanisms. For the best performance the wall properties of the fibre-composite anisotropic walls should probably be such that the wall displacement parallel to the fibre direction is as small as possible. In the case of isotropic walls horizontal displacement was found not to have a detrimental effect on the growth of the Tollmien–Schlichting waves, but this result is considered rather unreliable. The greater the wall displacement in the direction parallel to the fibres the less the difference in performance between walls with positive and negative fibre angles.

The optimal properties of anisotropic compliant walls are such that the walls are lighter and the elastic modulus lower than the corresponding isotropic walls. Nevertheless these properties appear to be practically realizable at flow speeds of 20 m/s in water.

Damping in the wall has a more deleterious effect on the growth of the Tollmien–Schlichting waves for anisotropic compliant walls than for the isotropic case.

The application of global convergence methods has led to the discovery of an anomalous spatially growing eigenmode which, according to conventional interpretation, would represent an instability. Further study of an appropriate initial-value problem revealed that for compliant walls complex wavenumbers with positive real parts and negative imaginary parts do not necessarily correspond to an instability. Accordingly, the new eigenmode probably does not constitute an instability. However, the associated eigenvalues are sufficiently close to the conventional ones to cause confusion.

This paper was written while Dr Carpenter was on study leave at the Department of Aerospace Engineering, The Pennsylvania State University. He would like to

express his gratitude to that institution and the Office of Naval Research for their financial support. The work is part of a research programme at the University of Exeter which is supported by the Ministry of Defence (Procurement Executive). The authors would also like to express their appreciation for the extensive numerical data supplied by R. D. Joslin (Pennsylvania State University).

REFERENCES

BABENKO, V. V. & SURKINA, P. M. 1969 Some hydrodynamic features of dolphin swimming. *Bionika* **3**, 19–26 (in Russian).

BELLMAN, R. E. & KALABA, R. E. 1965 *Quasilinearization and Boundary-Value Problems.* American Elsevier.

BENJAMIN, T. B. 1959 Shearing flow over a wavy boundary. *J. Fluid Mech.* **6**, 161–205.

BENJAMIN, T. B. 1960 Effects of a flexible boundary on hydrodynamic stability. *J. Fluid Mech.* **9**, 513–532.

BENJAMIN, T. B. 1963 The threefold classification of unstable disturbances in flexible surfaces bounding inviscid flows. *J. Fluid Mech.* **16**, 436–450.

BRIDGES, T. J. & MORRIS, P. J. 1984 Differential eigenvalue problems in which the parameter appears nonlinearly. *J. Comput. Phys.* **55**, 437–460.

BRIGGS, R. J. 1964 Electron-Stream Interaction with Plasmas. MIT Press.

CARPENTER, P. W. 1984*a* The effect of a boundary layer on the hydroelastic instability of infinitely long plates. *J. Sound Vib.* **93**, 461–464.

CARPENTER, P. W. 1984*b* A note on the hydroelastic instability of orthotropic panels. *J. Sound Vib.* **94**, 553–554.

CARPENTER, P. W. 1984*c* The hydrodynamic stability of flow over non-isotropic compliant surfaces. *Bull. Am. Phys. Soc.* **29**, 1534.

CARPENTER, P. W. 1985*a* Hydrodynamic and hydroelastic stability of flows over non-isotropic compliant surfaces. *Bull. Am. Phys. Soc.* **30**, 1708.

CARPENTER, P. W. 1985*b* The optimization of compliant surfaces for transition delay. *University of Exeter, School of Engineering, Tech. Note* 85/2.

CARPENTER, P. W. 1987*a* The optimization of compliant surfaces for transition delay. In *Proc. IUTAM Conf. on Turbulence Management & Relaminarisation, Bangalore, India* (ed. H. W. Liepmann & R. Narasimha), pp. 305–313. Springer.

CARPENTER, P. W. 1987*b* The hydrodynamic stability of flows over simple non-isotropic compliant surfaces. In *Proc. Intl Conf. on Fluid Mech., Beijing, China*, pp. 196–201. Peking University Press.

CARPENTER, P. W. 1990 Status of transition delay using compliant walls. In *Viscous Drag Reduction in Boundary Layers* (ed. D. M. Bushnell & J. N. Heffner), pp. 79–113. AIAA.

CARPENTER, P. W. & GAJJAR, J. S. B. 1990 A general theory for two- and three-dimensional wall-mode instabilities in boundary layers over isotropic and anisotropic compliant walls. *Theor. Comput. Fluid Dyn.* 2.

CARPENTER, P. W. & GARRAD, A. D. 1985 The hydrodynamic stability of flows over Kramer-type compliant surfaces. Part 1. Tollmien–Schlichting instabilities. *J. Fluid Mech.* **155**, 465–510.

CARPENTER, P. W. & GARRAD, A. D. 1986 The hydrodynamic stability of flows over Kramer-type compliant surfaces. Part 2. Flow-induced surface instabilities. *J. Fluid Mech.* **170**, 199–232.

CARPENTER, P. W., GASTER, M. & WILLIS, G. J. K. 1983 A numerical investigation into boundary layer stability on compliant surfaces. In *Numerical Methods in Laminar and Turbulent Flow*, pp. 166–172. Pineridge.

CARPENTER, P. W. & MORRIS, P. J. 1985 The hydrodynamic stability of flows over non-isotropic compliant surfaces. Numerical solution of the differential eigenvalue problem. In *Numerical Methods in Laminar and Turbulent Flow*, pp. 1613–1620. Pineridge.

CARPENTER, P. W. & MORRIS, P. J. 1989 Growth of three-dimensional instabilities in flow over compliant walls. *Proc. 4th Asian Cong. of Fluid Mech., Hong Kong*, pp. A206–209.

DANIEL, A. P., GASTER, M. & WILLIS, G. J. K. 1987 Boundary layer stability on compliant surfaces. *British Maritime Technology Ltd., Teddington, UK, Final Rep.* 35020.

DENNIS, J. E., TRAUB, J. F. & WEBER, R. P. 1978 Algorithms for solvents of matrix polynomials. *SIAM J. Numer. Anal.* **15**, 523–533.

DOMARADZKI, J. A. & METCALFE, R. W. 1987 Stabilization of laminar boundary layers by compliant membranes. *Phys. Fluids* **30**, 695–705.

DUNCAN, J. H. 1988 The dynamic of waves at the interface between a two-layer viscoelastic coating and a fluid flow. *J. Fluids Structures* **2**, 35–51.

DUNCAN, J. H., WAXMAN, A. M. & TULIN, M. P. 1985 The dynamics of waves between a viscoelastic coating and a fluid flow. *J. Fluid Mech.* **158**, 177–197.

FFOWCS WILLIAMS, J. E. 1964 Reynolds stress near a flexible surface responding to unsteady air flow. *Bolt, Berenek and Newman Inc., Cambridge, Mass., Rep.* 1138.

FRASER, L. A. & CARPENTER, P. W. 1985 A numerical investigation of hydroelastic and hydrodynamic instabilities in laminar flows over compliant surfaces comprising one or two layers of visco-elastic material. In *Numerical methods in Laminar and Turbulent Flow*, pp. 1171–1181. Pineridge.

GARRAD, A. D. & CARPENTER, P. W. 1982 A theoretical investigation of flow-induced instabilities in compliant coatings. *J. Sound Vib.* **85**, 483–500.

GASTER, M. 1965 On the generation of spatially growing waves in a boundary layer. *J. Fluid Mech.* **22**, 433–441.

GASTER, M. 1987 Is the dolphin a red herring ? In *Proc. IUTAM Conf. on Turbulence Management & Relaminarisation, Bangalore, India* (ed. H. W. Liepmann & R. Narisimha), pp. 285–304. Springer.

GROSSKREUTZ, R. 1971 Wechselwirkungen zwischen turbulenten Grenzschichten und weichen Wänden. *MPI für Strömungsforschung und der AVA, Göttingen, Mitt. No.* 53.

GROSSKREUTZ, R. 1975 An attempt to control boundary-layer turbulence with nonisotropic compliant walls. *University Sci. J. (Dar es Salaam)* **1**, 67–73.

JAFFE, N. A., OKAMURA, T. T. & SMITH, A. M. O. 1970 Determination of spatial amplification factors and their application to predicting transition. *AIAA J.* **8**, 301–308.

JORDINSON, R. 1970 The flat plate boundary layer. Part 1. Numerical integration of the Orr–Sommerfeld equation. *J. Fluid Mech.* **43**, 801–811.

JOSLIN, R. D. 1987 The sensitivity of boundary layer instability growth rates to compliant wall properties. M.S. thesis, Pennsylvania State University.

JOSLIN, R. D. & MORRIS, P. J. 1989 The sensitivity of flow and surface properties to changes in compliant wall properties. *J. Fluids Structures* **3**, 423–432.

JOSLIN, R. D., MORRIS, P. W. & CARPENTER, P. W. 1990 The role of three-dimensional instabilities in compliant-wall boundary-layer transition. *AIAA Paper* 90-0115.

KRAMER, M. O. 1960 Boundary layer stabilization by distributed damping. *J. Am. Soc. Naval Engrs* **72**, 25–33; *J. Aero/Space Sci.* **27**, 69.

LANDAHL, M. T. 1962 On the stability of a laminar incompressible boundary layer over a flexible surface. *J. Fluid Mech.* **13**, 609–632.

LUCEY, A. D. 1989 Hydroelastic instability of flexible surfaces. Ph.D. thesis, University of Exeter.

LUCEY, A. D., HARRIS, J. B. & CARPENTER, P. W. 1989 Three-dimensional hydroelastic instabilities of finite compliant panels. *Proc. 4th Asian Cong. of Fluid Mech., Hong Kong*, pp. I1–3.

MILES, J. W. 1957 On the generation of surface waves by shear flows. *J. Fluid Mech.* **3**, 185–199.

MILES, J. W. 1959*a* On the generation of surface waves. Part 2. *J. Fluid Mech.* **6**, 568–582.

MILES, J. W. 1959*b* On the generation of surface waves. Part 3. Kelvin–Helmholtz instability. *J. Fluid Mech.* **6**, 583–598.

MILES, J. W. 1962 On the generation of surface waves by shear flows. Part 4. *J. Fluid Mech.* **13**, 433–448.

MORRIS, P. J. 1976 The spatial viscous instability of axisymmetric jets. *J. Fluid Mech.* **77**, 511–529.

MORRIS, P. J. 1986 Applications of matrix factorization in hydrodynamic stability. In *Trans. Fourth Army Conf. on Applied Maths and Computing*, pp. 53–66.

PRANDTL, L. 1921 Bermerkungen über die Enstehung der Turbulenz. *Z. Angew. Math. Mech.* **1**, 431–436.

SEN, P. K. & ARORA, D. S. 1988 On the stability of laminar boundary-layer flow over a flat plate with a compliant surface. *J. Fluid Mech.* **197**, 201–240.

SMITH, A. M. O. & GAMBERONI, H. 1956 Transition, pressure gradient and stability theory. *Douglas Aircraft Co., Long Beach, Calif. Rep.* ES26388.

STUART, J. T. 1958 On the non-linear mechanisms of hydrodynamic stability. *J. Fluid Mech.* **4**, 1–21.

WILLIS, G. J. K. 1986 Hydrodynamic stability of boundary layers over compliant surfaces. Ph.D. thesis, University of Exeter.

YEO, K. S. 1986 The stability of flow over flexible surfaces. Ph.D. thesis, University of Cambridge.

YEO, K. S. 1988 The stability of boundary-layer flow over single- and multi-layer viscoelastic walls. *J. Fluid Mech.* **196**, pp. 359–408.

YEO, K. S. 1990 The hydrodynamic stability of boundary-layer flow over a class of anisotropic compliant walls. *J. Fluid Mech.* (in press).

YEO, K. S. & DOWLING, A. P. 1987 The stability of inviscid flows over passive compliant walls. *J. Fluid Mech.* **183**, 265–292.